**Dissertation**

# Numerical Analysis on the Effect of J-groove on Flows around Rotating Disk and Casing

# 回転円板とケーシングの間の流れに対する **J-groove** 効果の数値解析

**Graduate School of Engineering Science**
**Yokohama National University**

**NGUYEN VO DAO**
グエンボダオ

**April 2022**

## Abstract

During operation and working of turbo machines such as centrifugal pumps and Francis turbines, axial thrust balancing is important. It is the summation of unbalanced impeller forces acting in the axial direction. Pressure fluctuations occur at the interface between the rotor and stator. This rotor-stator interaction may be responsible for fatigue damage and cracks. To control and balance the axial thrust, a very simple method using shallow radial grooves mounted on the casing wall, called “J-groove”, was proposed, and studied experimentally. The main design criteria for the J-Groove are number, depth, length, and width. This thesis presents a numerical study of the effect of J-groove on the flow in the various gap along enclosed rotating disks based on open-source CFD software. Computational fluid dynamics (CFD) over the past decades has allowed large and complex simulations to be performed in reasonable time, thereby reducing the pre-project budgets largely. Furthermore, it has proven to be a powerful research tool when examining the complex problems and interplay of many phenomena, particularly in turbo machines. This study has improved the current understanding of the remarkable effect of J-groove. It is seen that the difference in pressure between the hub and shroud tip is changed with the changing number, depth, width, and length of J-groove.

Calculations were performed using the Navier-Stokes Equation solver available in OpenFOAM, an open-source Fluid Dynamics software. Furthermore, the code used in this thesis is open source which is obviously an advantage over commercial code. The modeled using Reynolds Averaged Navier Stokes (RANS) models was mostly k- ω SST as it predicted the outcome in the case without J-groove giving results close to the empirical value.

This dissertation consists of seven chapters, and the outline of each chapter is given below.

Chapter 1 clarified the position of this research by stating the background and purpose of this research and clarifying the research subjects.

Chapter 2 briefly presents the basic equations as well as the implementation in OPENFOAM for this thesis.

Chapter 3 presented the validation of turbulence models and the mesh independence, compared with the experimental results in the case of No groove.

Chapter 4 contains the fundamental characteristics of flow in different gaps between rotating disk and casing without through-flow. Theoretical analysis of effect of J-groove its parameters.

Chapter 5 presents the characteristics of flow in different gaps between rotating disk and casing with inward through-flow. Theoretical analysis of effect of J-groove its parameters.

Chapter 6 describes the estimation of effect of J-groove with various parameters. Determination of optimum J-groove dimension and give the brief determination of for future research.

Chapter 7 summarizes the results obtained in this research and describes future prospect.

## Content

# Nomenclature

(Unless otherwise mentioned, the followings are the meaning)

| | |
|---|---|
| $r_1$, $r_2$ | inner, outer radius [mm] |
| $\Omega$ | angular velocity of rotor [rad/s] |
| $\rho$ | fluid density |
| $\upsilon$ | kinematic laminar viscosity |
| $\upsilon_t$ | kinematic turbulent viscosity |
| $Re$ | Reynolds number ($= \omega r_2^2/\upsilon$) |
| $Cp$ | pressure coefficient ($=2(p - p_2)/ \rho r_2^2 \omega^2$) |
| $h$ | axial gap [mm] |
| $S$ | axial gap radius ratio ($=h/r_2$) |
| $v$, $u$ | radial and tangential velocity |
| $R$ | radius ratio ($=r/r_2$) |
| $n$ | number of J-grooves |
| $w$, $l$, $d$ | width, length, depth of J-groove [mm] |
| $D$ | dimensionless depth ratio ($=d/r_2$) |
| $W$ | dimensionless width ratio ($=w/r_2$) |
| $L$ | dimensionless length ratio ($=l/r_2$) |
| $z$ | distance from the rotating wall [mm] |
| $Z$ | dimensionless distance from rotor wall ratio ($=z/h$) |
| $C_q$ | flow rate coefficient |
| $C_t$ | axial thrust coefficient |
| $\Delta C_t$ | axial thrust reduction ratio |
| $\omega$ | turbulent dissipation rate |
| $k$ | turbulent energy k |

## List of Figures

# List of Tables

# Chapter 1

# Introduction

## Chapter 1: Introduction

### 1.1 Bibliographic Review

Turbomachinery plays a very important role in industry, in supplying and moving the world's energy. From a technical perspective, its applications can be divided into 2 types of fluid flows: compressible and incompressible flows. This work only involves incompressible flow. Most pumps operate at high Reynolds

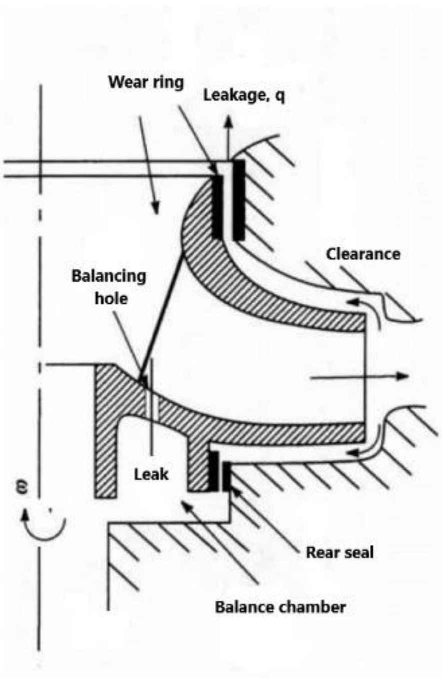


*Fig. 1.1 leakage flow associated with a typical centrifugal pump*

numbers, and leakage flow associated with a typical centrifugal pump in this flow regime most hydraulic losses occur due to secondary flow and turbulent mixing as shown in Fig. 1.1. Different pressure levels across the fluid contact areas within the gap between the rotor and stator cause axial forces. To reduce forces on bearings already subjected to high loads, axial thrust must be accurately predicted and minimized by design.

For the subject of the flow cavity between a finite rotation and the stationary disks, most of the research has been done theoretically and experimentally on incompressible viscous medias working between parallel walls. Due to centrifugal force, the pressure in the cavities between the stator and the rotor on both its sides typically decreases from a high impeller outlet pressure at the outer radius of the impeller to a lower pressure level towards the center. Measures to balance axial forces usually aim to change the pressure distribution on the backside of the impeller so that there is an equilibrium under steady state conditions. There are some methods of balancing the axial thrust such as balancing disk, balancing hole, and sealing. However, many of these devices have become complicated and

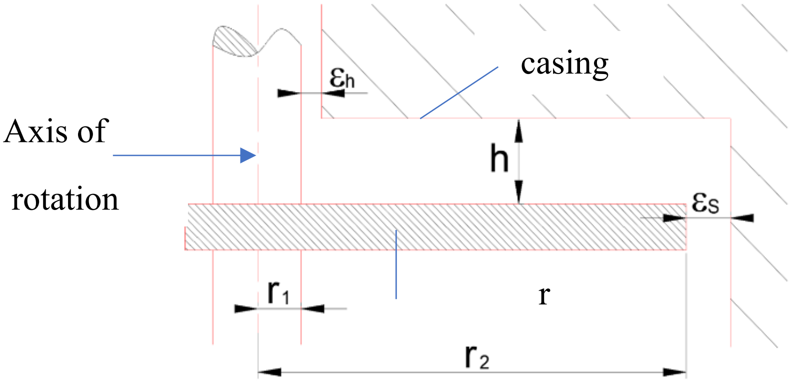


*Fig. 1.2 geometrical configuration rotating disk model*

sometimes cause problems like vibration due to the balancing disk. Kurokawa and his collaborators developed a straightforward method where shallow radial grooves, called “J-groove”, were mounted on the casing wall of the main impeller proved a remarkable effect on decreasing the radial pressure drop, which increased the axial force towards discharge resulting in a large decrease in total axial thrust.

The study of Theodore Von Karman in 1921 is one of the earliest basic references to the analysis of a flow over a free rotating disk. The hydrodynamic initial characteristics of a flow and frictional resistance of enclosed rotating disks were reported by Daily and Nece in 1960. A fundamental criterion for the application of rotor casing treatment and the stability of pumping systems were investigated by Greitzer.

In centrifugal turbo machines, the fluid leakage flow from the outer radius of the impeller to the impeller-hub, which has a major impact on the radial pressure distribution and axial thrust.

The geometrical configuration for the case without and with J-groove are shown in Fig. 1.2 and Fig. 1.3, respectively.

The rotor-stator system, depicted in Figure 1, is a simple model of the current investigated in this paper. It is made up of a cylindrical cavity that is surrounded by a stationary disk (stator) and a smooth rotating disk (rotor). The cavity is surrounded by a fixed shroud.

J-groove is mounted on the casing wall. The J-Groove is a rectangular groove, and its main parameters are the number *n*, the depth (*D*), the length (*L*) and the width (*W*).

Recent research on J-groove shows that shallow grooves can drastically reduce swirl strength in the axial gap flow between the shroud and the casing wall. By this swirl reduction effect, the radial pressure distribution curve is flattened, and the axial thrust is significantly reduced. However, the reason for this effect and its optimum parameter is not clear. The design parameters of the J-Groove have not been clarified in previous studies. Therefore, the influence of different design parameters was observed in this thesis.

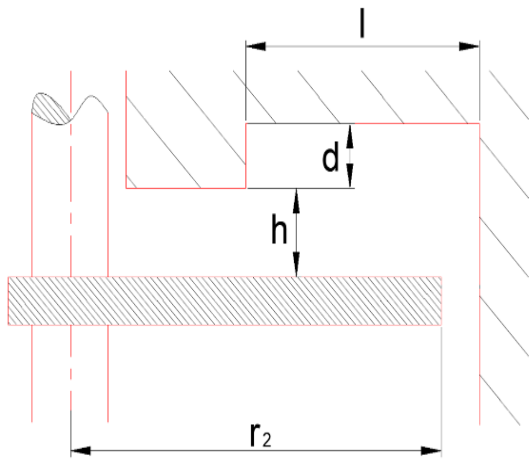


*Fig. 1.3 geometrical configuration for J-groove*

## 1.2 Short Work Overview

There is a great deal of scope and research prospect in Turbine Machinery Axial Force Control. However, there are limited investigations using advanced turbulence models such as Large Eddy Simulation (LES), Detached Eddy Simulation (DES) and Direct Numerical Simulation (DNS). The present doctoral thesis is more focused on establishing the computational basis to go further by providing a perfect understanding of the effect of the J-groove parameters on the reduction of axial thrust.

### 1.3 Dissertation Outline

The content of this dissertation is documented mainly in six chapters.

The first chapter is Introduction to current dissertation mainly divided into four topics with Bibliographic review, Overview and scope of current work, and outline of chapters.

Chapter 2 covers numerical analysis including continuous momentum equations and Navier-Stokes solved with computational tools to deal with flow phenomena. Turbulence model considered in this thesis k- ω SST is drafted briefly. In addition, the solving process used in the OpenFOAM solver for this thesis is mainly SimpleFoam using the built-in SIMPLE algorithm.

Chapter 3 covers Validation and Testing of Parameters in OpenFOAM. This is the first part of the Results and Discussion obtained from this thesis. All the parameters mentioned in the sub-objective are different and the results and discussion are provided in this chapter. Next is the result of confirming the calculation results with experimental data.

Chapter 4 covers the results obtained from changing the J-groove parameters, calculated for each parameter on the flow in different gaps without through-flow. All the parameters mentioned in the main objective that play an important role in the flow are considered. The determination of hydraulic loss caused by J-groove.

Chapter 5 focuses on the effect of J-groove on the flow in various gaps with through-flow. The pressure distribution of gap flow imposed with radial through-flow from a narrow gap to a large gap.

Chapter 6 describes the estimation of effect of J-groove with various parameters without and with through-flow for narrow, intermediate, and relatively large gaps and contains the fundamental characteristics of the application of J-groove. An innovative and simple method of using shallow grooves mounted on the casing wall.

Chapter 7 focuses on the conclusions of the results obtained from Chapters 3, 4, 5, and chapter 6 along with future work that will be done to prepare this thesis into research publications and as recommendations common to the research community.

Next will be all the References and Appendix.

# Chapter 2

# Numerical Methods

# Chapter 2: Numerical Methods

The purpose of this chapter is to introduce the theory used in this study. It starts with the Governing equation. Then an introduction to turbulence models will be presented. Furthermore, other methods as well as some basic numerical methods, parallel scalability studies and Open-Water characteristics will be discussed briefly. Besides, a basic overview of the implementation of OpenFOAM also are shown.

## 2.1 Basis Equations

### 2.1.1 The governing equations

The equations governing Newtonian fluid flow can be found in numerous fluid mechanics textbook.

In addition to the assumptions used to derive these equations, the following assumptions are made for this thesis:

1. Steady state conditions
2. Incompressible flow

With these assumptions, the basic governing equations for the incompressible flow are continuity and the momentum equations are introduced in Eq. (2.1) and (2.2), respectively for i component of momentum, i =1 to 3:

$$\frac{\partial u_i}{\partial x_i} = 0 \qquad (2.1)$$

$$u_j \frac{\partial u_i}{\partial x_j} = -\frac{1}{\rho}\frac{\partial p}{\partial x_i} + \frac{\partial}{\partial x_j}\left[(\upsilon + \upsilon_t)\left(\frac{\partial u_i}{\partial x_j} + \frac{\partial u_j}{\partial x_i}\right)\right] \qquad (2.2)$$

where $p$ is the pressure, $u$ is the velocity, $\upsilon$ is the laminar viscosity, and $\upsilon_t$ is the turbulent viscosity.

Since the density is assumed to be constant and hence no need to distinguish the constant. Writing continuity equations in this form ensures that mass is conserved for these types of flows.

Equations (2.1), (2.2) apply directly to laminar flows. However, for turbulent flows, time average equations are solved.

### 2.1.2 Turbulent flows and turbulence modelling

The governing equations (2.3) and (2.4) are solved by the finite volume method (FVM). The FVM is mainly used in commercial and open-source CFD software. It is the most natural discretization scheme because it makes use of the conservation laws in integral form. It subdivides the domain into cells and evaluates the field equations in integral form on these cells.

In general, the FVM-based CFD solver is developed in space and time with the following steps for the conservative equation of a variable. However, detailed equations for this thesis are:

- Integrate conservation equations in each cell.
- Calculate the face value according to the value of the center of the cell. (Cell-center).
- Set of physical variables or parameters overall repeatability for steady-state simulation.

OpenFOAM (version 8) is used to solve the governing Eq. (2.1) and (2.2). Although there are many turbulence models available in OpenFOAM, it should be clear that the availability of computational resources and simulation time play an important role in the selection of high accurate turbulence models.

Among the turbulence models below, RANS is a modelling approach to predict turbulent flows by averaging the Navier-Stokes equations. This thesis uses the RANS turbulence model mainly the *k- ω* SST turbulence model. This is the best RANS model available for near wall treatment. The *k- ω* SST model with equations for k and ω with other parameters for calculating turbulent viscosity is available in Menter's k- ω SST. The transport equations for *k* and *ω:*

$$\frac{\partial k}{\partial t} + U_j \frac{\partial k}{\partial x_j} = P_k - \beta^* k\omega + \frac{\partial}{\partial x_j}\left[(\nu + \sigma_k \nu_t)\frac{\partial k}{\partial x_j}\right] \tag{2.3}$$

$$\frac{\partial \omega}{\partial t} + U_j \frac{\partial \omega}{\partial x_j} = \alpha S^2 - \beta\omega^2 + \frac{\partial}{\partial x_j}\left[(\nu + \sigma_\omega \nu_t)\frac{\partial \omega}{\partial x_j}\right] + 2(1 - F_1)\sigma_{\omega^2}\frac{1}{\omega}\frac{\partial k}{\partial x_i}\frac{\partial \omega}{\partial x_i} \tag{2.4}$$

The two variables that are transported are the turbulence kinetic energy ($k$), which defines the energy in the turbulence, and the specific turbulence dissipation rate ($\omega$), which determines the rate of dissipation per unit of turbulence kinetic energy. SST stands for shear stress transport. The SST formula converts to $k$-$\epsilon$ behavior in the free-stream, which avoids the $k$-$\omega$ problem that is sensitive to the turbulence characteristics of the input free-stream. For $k$- $\omega$ SST model, the k and ω will be calculated from the turbulent intensity I and turbulence length scale l. In short, the following expressions will be used to calculate the parameters turbulence.

The turbulent flow intensity ($I$) for a fully developed flow can be estimated as follows:

$$I = 0.16Re_{d_h}^{-1/8} \quad (2.5)$$

where $Re_{d_h}$ is the Reynolds number for a hydraulic diameter $d_h$.

The turbulence length in this case is

$$l = 0.07d_h \quad (2.6)$$

The turbulent energy k is given by:

$$k = \frac{3}{2}(UI)^2 \quad (2.7)$$

The intensity indicates the turbulence level and can be determined as follows:

$$I = \frac{u'}{U} \quad (2.8)$$

where $u'$ is the root-mean-square of the turbulent velocity fluctuations, given as:

$$u' = \sqrt{\frac{1}{3}\left({u'_x}^2 + {u'_y}^2 + {u'_z}^2\right)} = \sqrt{\frac{2}{3}k} \quad (2.9)$$

The mean velocity U can be calculated:

$$U = \sqrt{\left(U_x^2 + U_y^2 + U_z^2\right)} \quad (2.10)$$

The specific turbulent dissipation rate can be calculated by the following formula:

$$\omega = C_\mu^{3/4}\frac{k^{1/2}}{l} \quad (2.11)$$

where $C_\mu$ is the turbulence constant usually taking the value 0.09.

The turbulent viscosity is calculated as follows:

$$\nu_t = \frac{k}{\omega} \quad (2.12)$$

### 2.1.3 Theoretical analysis in the case of J-groove

Kurokawa et al. studied with an enclosed rotating disk, which displaces the flow between the casing wall and the impeller housing. Even using the CFD code, it is still difficult to calculate the axial thrust with great accuracy. To better understand the flow in the stator-rotor cavity, the momentum integration method by assuming the logarithmic law as the gap flow profile is applied. In general, there are two types of gap flow. One is the "non-interfered gap flow" which is widely used in many cases, and the other is the "interfered gap flow", shown in Fig. 2.1 and 2.2. The former is a flow consisting of boundary layer on both wall rotor-stator and core flow where tangential velocity $v_\theta$ is expressed in $K.r.\omega$ and no radial flow exists. But in the latter, the core flow disappears, and the boundary layers interfere with each other due to a very narrow gap or caused by superimposed radial flow. In both types of flow, the flow characteristic is determined from the momentum, angular momentum and continuity equations shown as follows:

$$\frac{\partial}{\partial r} r \int_0^h v^2 dz - \int_0^h u^2 dz = -\frac{r}{\rho}\frac{\partial p}{\partial r} h - \frac{r}{\rho}(\tau_{s\theta} + \tau_{r\theta}) \quad (2.13)$$

$$\frac{\partial}{\partial r}\int_0^h r^2 uvdz = -\frac{r^2}{\rho}(\tau_{s\theta} + \tau_{r\theta}) \quad (2.14)$$

$$\int_0^\theta vdz + \int_0^\delta v'dz = \frac{Q}{2\pi r} \quad (2.15)$$

where $r$ and $z$ are radial and axial, $u$ and $v$ are tangential and radial velocities, $p$ is pressure, $\rho$ is the density of the fluid, $\tau_r$ and $\tau_s$ are shear stresses of the rotating and stationary walls. Q is the axial flow rate. The subscripts $r$ and $\theta$ are radial and tangential components, respectively.

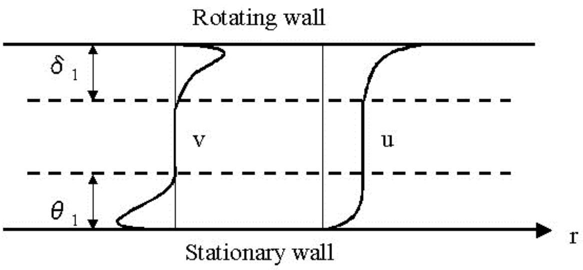

*Fig. 2.2 flow model of non-interfered gap*

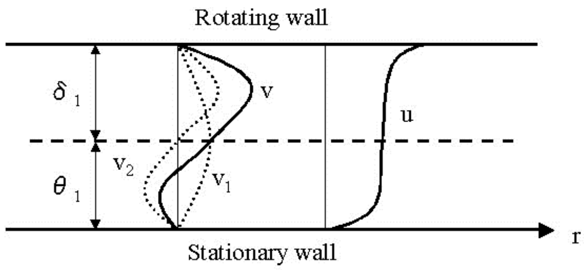

*Fig. 2.1 flow model of interfered gap flow*

When the J-groove is mounted on the stator wall, a radial flow is induced in the shallow groove due to the pressure gradient. The groove flow causes the outward flow along the rotating disk to increase to satisfy the continuity equation, which is:

$$\int_0^\theta vdz + \int_0^\delta v'dz = Q + Q_g \quad (2.16)$$

where $Q$ and $Q_g$ are radial flow rate in the axial gap between rotating disk and stationary wall and the flow rate in the J-grooves, respectively. The groove flow in J-groove case is determined by the radial balance as follow:

$$\tau_r dr = 4 r_h dp \tag{2.17}$$

where $\tau_r$ and $r_h$ are shear stress to radial direction and hydraulic radius of the J-groove, respectively.

From equation (2.17), the pressure distribution can be determined as follows:

$$\frac{dC_p}{dR} = 2K^2 R + 2R\left(\frac{C_q}{R^2 S}\right)^2 \tag{2.18}$$

where $C_p$ is defined as $C_p = 2(p - p_2)/\, \rho r_2^2 \Omega^2$, $p_2$ is the pressure at $r = r_2$.

The axial force working on each side of the impeller can by determined by integrating the pressure distribution as shown below:

$$F = \int_{r_1}^{r_2} 2\pi r p(r) dr = C_F . \rho \pi r_2^4 \Omega^2 \tag{2.19}$$

where $r_1$ and $r_2$ are the inner and outer radius of the impeller, respectively. $C_F$ in this formula is the axial force coefficient.

The total axial thrust T is given by the difference of axial forces $F_F$, $F_R$ on front and rear shroud and momentum change of the inlet flow working on the impeller as below:

$$T = F_R - F_F - \rho Q v \tag{2.20}$$

where $Q$ is main flow rate and $v$ is flow velocity at the mouth of the impeller.

### 2.2 Simulation setup in OpenFOAM

While a detailed analysis of the openFoam is beyond the scope of this thesis, it is important to outline some of the more common simulation setup in openFoam that occur in this study. The working fluid in this thesis is water, and outlet pressure is set to 0 bar. A computational domain is modeled using structured grids. This section provides guidance on the most appropriate way to determine boundary values.

#### 2.2.1 Meshing

It is important to reduce the cell size enough to reduce the error enough. However, if the cell size is reduced too much, the number of cells will become too large and will increase the calculation time. Therefore, a thorough analysis of the resolution of the mesh is key to quickly identifying a computational problem.

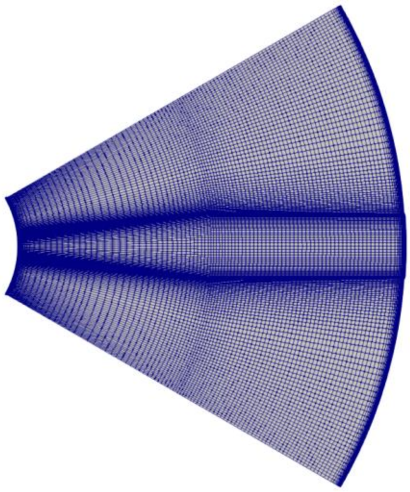

*Fig. 2.3 mesh computational domain in blockMesh case*

Figure (2.3) depict the computational domain used for this thesis by using blockMesh, respectively. They are created as in Appendix A.1.

Due to the domain, the grid has bounded boundaries equal to inlet, outlet, wall rotor, wall stator, and 2 periodic sides. The boundaries are as marked in Fig 2.4 below. The simple geometrical configuration sketched in Fig. (1.1) for the case without groove is composed of two smooth parallel disks with outer radius $r_2$= 150 mm and inner radius $r_1$= 30 mm separated by an axial gap $h$. The rotor and the hub attached to it rotate at the same rotational speed 750 rpm (i.e., angular velocity ω =78.5 rad/s), corresponding to the Reynolds number $Re = \Omega r_2^2/\nu = 1.73 \times 10^6$ ,

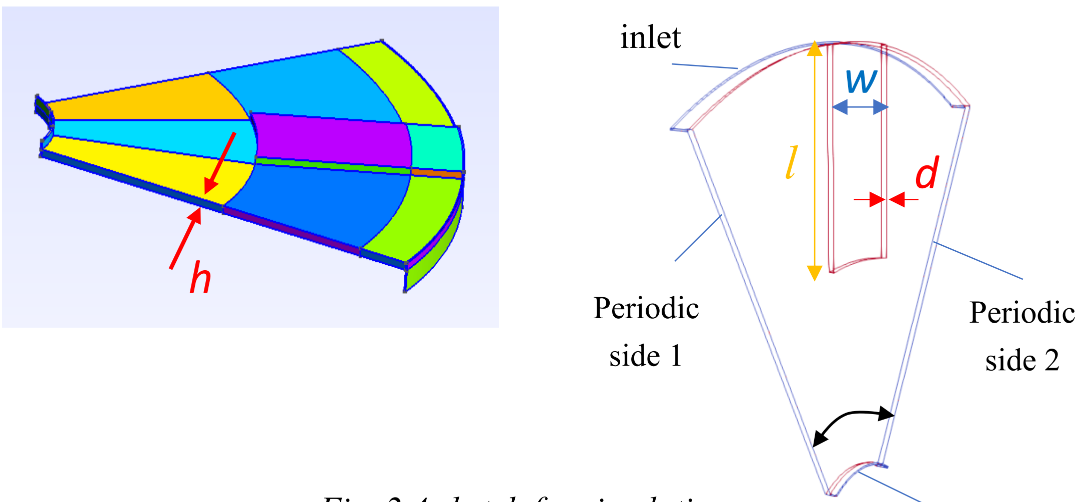


*Fig. 2.4 sketch for simulation case*

while the stator and the shroud are stationary. The axial gap between the rotating disk and the stationary wall is $h$ = 0.75mm (narrow gap); $h$ = 1.7 mm (intermediate gap), and $h$ = 8.34 mm (large gap), corresponding to the axial gap radius ratio $S = h/r_2$= 0.005; $S$ = 0.0113, and $S$ = 0.0556. The radial gap at the hub tip and the shroud tip are equal $\varepsilon_s = \varepsilon_h$ = 0,5 mm.

Figure (2.5) shows part of the 3-D mesh used in the computational model for the J-groove case. One single J-groove sector was selected, and the periodic rotation symmetry boundary condition was applied. In terms of boundary conditions, the rotating disk and hub attached to it were the rotor wall and the stationary disk and shroud were the stator wall. the shroud tip was the inlet while the hub tip was the outlet of the flow. The calculation area is divided into the inlet, rotor wall, stator wall, outlet and 2 periodic sides. The periodic boundaries of this sector lie mid-way between the J-grooves. This grid has proven to be sufficient to provide grid-independent solutions. The mesh has been refined at the rotor and the stator to resolve boundary layers.

### 2.2.2 Solver Setup in OpenFOAM

This section presents a brief overview of the implementation of OpenFOAM version 8 for 2 cases, with and without J-groove. In addition, the meshing strategy used blockMesh in OpenFOAM is covered in section (2.3.1). This will be helpful to anyone who is carrying out or continuing the work already done on the current thesis for the future.

OpenFOAM is a free and open-source CFD software package developed by Open CFD Ltd at ESI Group and distributed by the OpenFOAM Foundation. Parameters in openFoam are easily defined due to the perfectly organized case structure as shown in Figure (2.4) for k- ω SST turbulence model.

```
├── 0
│   ├── k
│   ├── nut
│   ├── omega
│   ├── p
│   └── U
├── constant
│   ├── polyMesh
│   ├── transportProperties
│   └── turbulenceProperties
└── system
    ├── blockMeshDict
    ├── controlDict
    ├── decomposeParDict
    ├── fvSchemes
    └── fvSolution
```

*Fig. 2.5 Case structure in OpenFOAM*

Figure 2.5 shows the case simulated in OpenFOAM. In summary, directory 0 represents the boundary conditions of the parameters at all boundaries with the initial values of the parameters mentioned under the "0" sign in Fig. 2.4 at time 0. Constant directory contains a complete description of the case mesh for this simulation in the *polyMesh* subdirectory and the 2 other files specifying the physical properties in the *transportProperties* and *turbulentProperties* files. The system directory is used to set parameters related to the solution process itself. It contains at least 3 *controlDict*, *fvSchemes* and *fvSolution* files as shown in the Appendix A5, A6 and A7.

a) Boundary conditions in directory 0

Directory 0 as shown in the Fig. 2.5 contains files to define boundary conditions and initial values for pressure (*p*) and velocity (*U*) common to any case simulation. Other parameters change depending on the turbulence model being performed which in this case is the k- ω SST model. The turbulence kinetic energy (*k)*, turbulent viscosity (*nut*) and the specific dissipation rate (*omega*) are determined respectively.

The pressure and velocity are determined as in Appendix A.3. The pressure is declared as zeroGradient at the inlet, wallStator as well as wallRotor. The outlet is initialized to a uniform value of zero, compared to atmospheric pressure in the OpenFOAM solver. The inlet flow rate is a fixed value by FlowRateInletVelocity. The outlet velocity is considered as the inlet and completely resolves the flow. The wall stator with a fixed velocity of zero. The speed of the wall rotor has a fixed value and is equal to 750 rpm (i.e., angular velocity Ω =78.5 rad/s), corresponding to the Reynolds number Re = $\Omega r_2^2/\nu = 1.73 \times 10^6$.

The boundary and initial conditions of k- ω SST model parameters are specified separately using *k*, *nut*, and *omega* as shown in Appendix A.4. The turbulence kinetic energy (*k*) is determined on the joining and initialization boundaries. The boundary conditions of *k* at the inlet with keyword TurbulentIntensityKineticEnergyInlet are declared as fixed values with initial values calculated from the numerical formulas defined in section (2.1.2). The specific dissipation rate (*omega*) is determined at all boundaries using the same physical phenomena mentioned in the turbulence kinetic energy boundary condition (*k*). Therefore, it is a fixed value in the inlet with a numeric value calculated from the mathematical expressions mentioned in section (2.2.1) with keyword TurbulentMixingLengthFrequencyInlet. The turbulent viscosity (*nut*) is not repeated in the computational simulation as it can be obtained from the (*k*) and the (*omega*) as mentioned in the mathematical expressions in section (2.2.1). It is therefore defined as a fixed value in the inner field, and the "calculated" OpenFOAM primitive type boundary condition of the computational domain.

For velocity components on solid surfaces, non-slip boundary conditions are used. With a defined mass flow rate, a uniform axial velocity is used, and the tangential velocity component is established to have pre-rotating flow at the inlet. To ensure continuity, the output uses a uniform axial velocity, and the tangential velocity is calculated from the zero normal derivative condition. At the input and output, the radial velocity component is set to zero. The detailed boundary conditions are shown in Table 3. It's worth noting that a peculiar boundary condition was applied to "on the rotor surface." The rotor is assumed to be the boundary because it is porous and the only input boundary. The equations are referred to as "input."

b) Turbulence Models

OpenFOAM provides a wide range of methods and models for turbulence simulation. The thesis focuses on using the Reynolds Averaged Navier Stokes (RANS) turbulence model or the RAS turbulence model. The best model available in the list of options in RAS models for better physical modeling of near-wall flow is k- ω SST, it has been chosen to simulate the cases in this thesis.

The turbulence model implementation must be done in two files namely turbulentProperties where the simulation type must be defined which in this case is the RAS Model. Then in the OpenFOAM RAS properties file, a specific RAS Model must be selected, whether turbulence is enabled or not. Two files, RAS Properties and Turbulence Properties, can be found in Appendix A.5. This is the same case with and without J-grooove.

c) ControlDict

The controlDict dictionary sets the required input parameters to create the database. Keyword entries can be found in references (the openFOAM User Guide). Below are the standard settings used in this thesis and also cited in Appendix A.6. Since it is a steady-state simulation, the endTime in controlDict shows the number of iterations instead of the time, and deltaT should be 1, since it is the iteration gain. Other parameters are described in detail in the OpenFOAM user guide or the references provided.

d) fvschemes

The fvSchemes dictionary in the system directory establishes numerical schemas for the derivative and interpolation terms along with the specification of the throughput requirement terms. Terms that normally must be assigned to a numeric schema in fvSchemes including gradient, divergence, and Laplacian, and time derivative terms along with interpolation terms for the value that will be interpolated from one set of points to another set of points as specified in Appendix A.7.

e) fvSolution

The equation solver, smoother, tolerance and algorithm are controlled from the fvSolution dictionary in the system directory. FvSolution contains a sub-dictionary specific to the solver being run. Depending on the solver selected in OpenFOAM, the fvSolution file must be modified with the parameters solved by that solver. In the present case, simpleFoam is used to solve steady-state cases. The fvSoltuion files are provided in Appendix A.8.

The first subdictionary in the fvSolution file requires *solvers* to be defined for the various parameters being analyzed. This usually includes pressure, velocity, and turbulence parameters such as *k* and *omega* in this thesis. Solver available in OpenFOAM as shown in the references along with the OpenFOAM User Guide.

The second fvSolution sub-dictionary commonly used in OpenFOAM is *relaxationFactors* that controls under-relaxation, a technique used to improve computer stability, especially in solving steady-state problems. The optimal choice of the relaxation coefficient is one that is small enough to ensure stable computation but large enough to move the iterative process quickly. In this thesis, in all cases, the simulation is monitored at runtime and the relaxation parameters are fixed with value 0.95.

The third dictionary is used to define the parameters algorithm. In general, the SIMPLE (Semi-Implicit Method for Pressure Linked Equation) algorithm is used for steady-state solvers and is selected in this thesis, while PISO and PIMPLE used for transient solvers.

All algorithms are based on evaluating some solutions initially and then correcting them. The number of non-orthogonal in this thesis is 0 and it is not changed at runtime in all cases.

More detailed information about the fvSolution file and its components can be obtained from the OpenFOAM User Guide or from the references.

### 2.3 Summary of Chapter 2

The present study gives the basic equations and simulation setup in the openFoam. Also, an introduction to turbulence models is presented. The boundary conditions for the flow field are summarized in table 2-1.

*Table 2-1 Boundary condition for CFD analysis*

| | |
|---|---|
| Calculation type | Steady state |
| Turbulence model | k- ω Shear Stress Transport |
| Inlet condition | Flow rate, |
| Outlet condition | Static pressure |
| Walls | No slip |

# Chapter 3

# Validation and computational testing

# Chapter 3: Validation and computational testing

## 3.1 Testing of computational parameters

Experimental data is available in reference from the results of Kurokawa et.al. as shown in Appendix B.1. Software WebPlotDigitizer 4.5 is used to get the result from that graph and compare it with the result from the CFD.

### 3.1.1 Variation of turbulence models

The turbulence was modeled only using the Reynolds Averaged Navier Stokes (RANS) or Reynolds Averaged Stress (RAS) models. There are many classes specific turbulence models available in OpenFOAM as mentioned in section (2.1.2) and (2.2.2).

Figure 1 depicts the model geometry. It is based on the experimental rotor-stator system used by Poncet et al. [18] in their measurement. The system is made up of a rotating disk (rotor) and a stationary disk (stator). The system is encased in a fixed shroud.

Three different turbulence models were examined to find the model which can best match the experimental data, without a J-groove situation. The graphs of the dimensionless radius ratio $R = r/r_2$ and the pressure coefficient $Cp$ in Fig. 3.1 show the pressure distribution along the radius for three different turbulence models together with the experimental results of Kurokawa et.al. $Cp$ is defined as

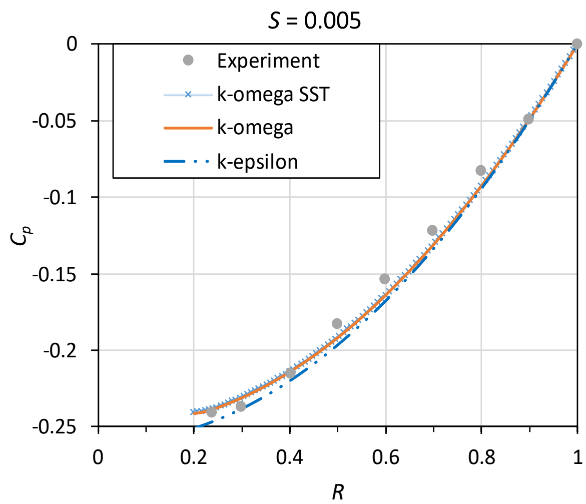


*Fig. 3.1 pressure distribution for S=0.005 using different turbulence models and comparison with experimental data.*

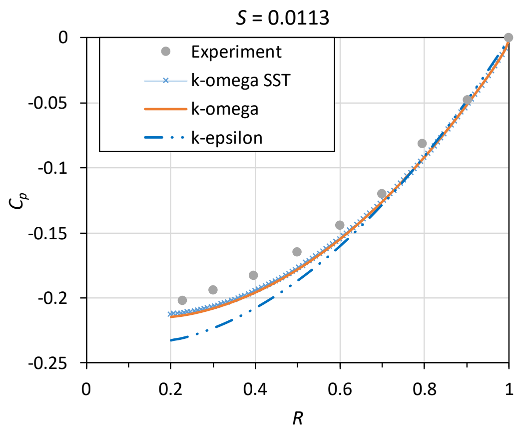


*Fig. 3.3 pressure distribution for S=0.0113 using different turbulence models and comparison with experimental data.*

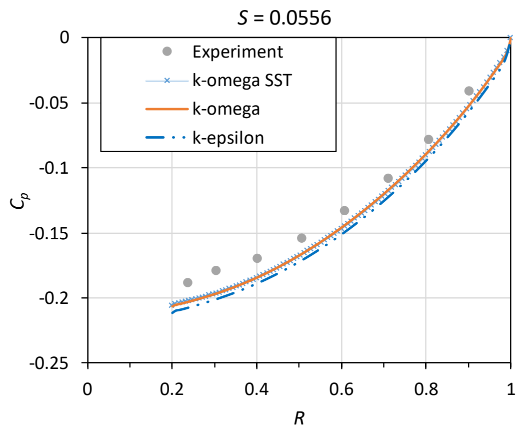


*Fig. 3.2 pressure distribution for S=0.0556 using different turbulence models and comparison with experimental data.*

$Cp = \frac{2(p-p_2)}{\rho r_2^2 \Omega^2}$, where $p_2$ is the pressure at $r = r_2$. As shown in Fig. 3.1, the two turbulence models k-omega and k-omega SST predict a similar pressure distribution across the radius of the impeller. However, there was a noticeable difference for the k-epsilon model between the predicted and experimental values. Moreover, as shown in Fig. 3.2 and Fig. 3.3, in another situation of gap ratio *S*, the k-omega SST also has an agreement with the experimental data. Consequently, the k-omega SST turbulent model is used for further simulation.

The idea is to create a better physical model for the flow near the wall. So, *k- ω* SST (shear stress transport - 2 equations) is used from the list of available turbulence models for incompressible flows. Although *k- ω* SST well-known models with near-wall processing in RANS turbulence models, it is better to evaluate the performance for the specific cases of this thesis.

### 3.1.2 Mesh independent

A computational domain is modeled using structured grids. Grid independence was confirmed by performing simulations on three consecutive grid refinements for the absence of J-groove case with 829808 elements (Mesh-1), 1270048 (Mesh-2) and 1808576 (Mesh-3). A comparison of pressure distributions using different mesh densities is shown in Fig. 3.3, where a strong agreement is observed among these three results. Mesh-1 was chosen for further simulation as a consensus between computational cost and accuracy. The CFD model was therefore validated.

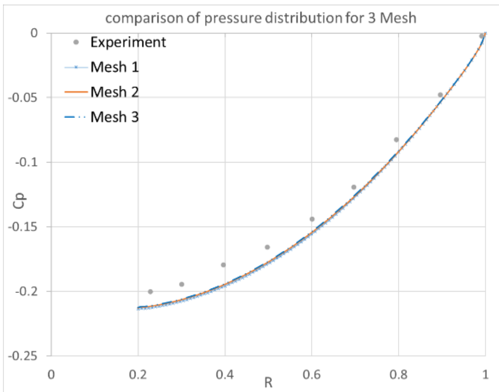


*Fig. 3.4 pressure distribution using different mesh densities and comparison with experimental data.*

### 3.2 Validation with Experimental results

To confirm the validity of the study, comparison of the CFD results and experimental results is shown in Fig. 3.4, 3.5 and 4.6. This section will show the comparison for all case $S = 0.005$; $S = 0.0113$; $S = 0.0556$ with through-flow also. There is no noticeable difference from the results without the J-groove.

One of the most influential parameters for flow problems in the rotor-stator cavity is the external leakage flow through the cavity. In general, the leak contains a tangential velocity component and thus creates an additional angular momentum. The influence of disk rotation is determined by the magnitude of the leakage flow.

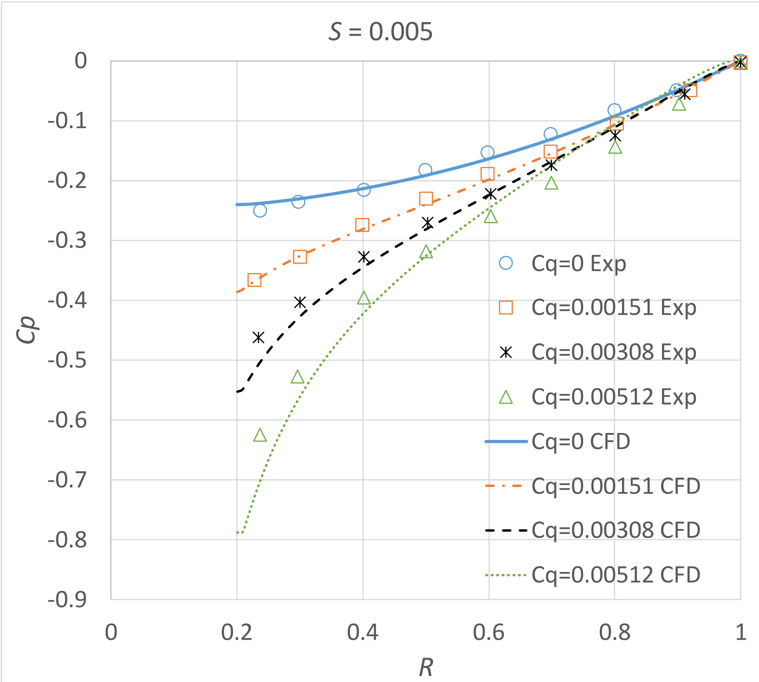


*Fig. 3.6 comparison of pressure distribution for S = 0.005*

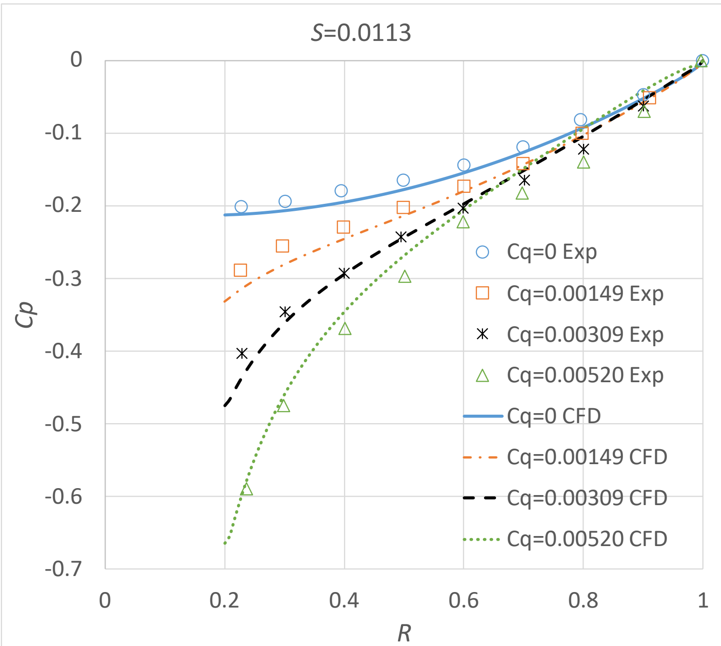


*Fig. 3.5 comparison of pressure distribution for S = 0.0113*

For all investigated flow rates, there are some deviations. SST modeling implemented in openFOAM is a good compromise in terms of prediction quality,

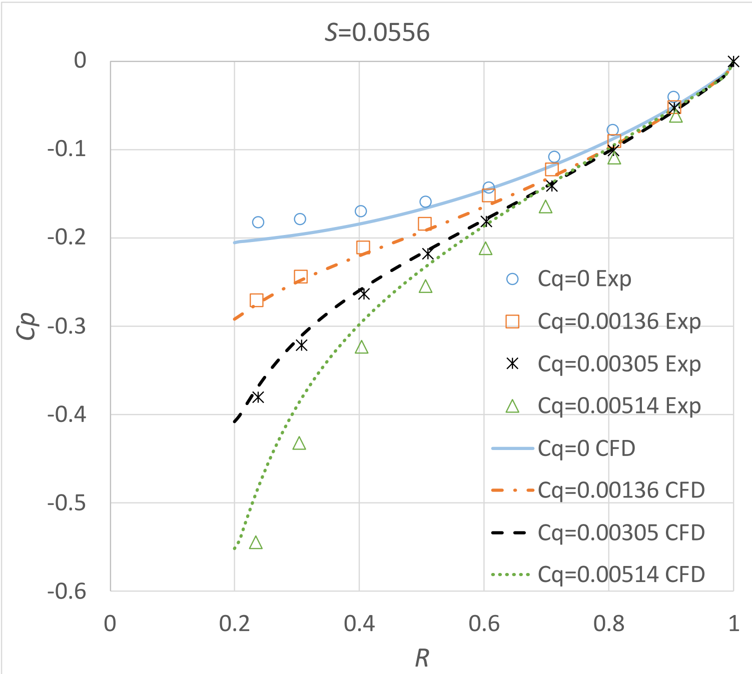


*Fig. 3.7 comparison of pressure distribution for S = 0.0556*

convergence, and modeling effort. The pressure drops increases with intensifying throughflow.

For the CFD analysis validation test with J-groove installation, the difference of axial thrust coefficient $\Delta C_t$ was investigated by experimental analysis, which comprised the CFD analysis result. The axial thrust coefficient is determined as following

$$C_t = \int_{r_1}^{r_2} C_p r dr \quad (3.1)$$

$$\Delta C_t = C_t - C_{t_{ng}} \quad (3.2)$$

, where $C_{t_{ng}}$ is the value of axial thrust coefficient in the case of without J-groove.

The experimental and CFD analyses were performed under a constant rotational speed with different flow coefficient $\phi = \frac{Q}{2\pi r_2 b_2 (r_2 \Omega)}$, where $Q$ is flow rate and $b_2$ is impeller width ($b_2$= 0.01 m). The CFD analysis result was consistent with the experiment result with a small deviation, as shown in Fig. 7 and Fig. 8. The margin of error is calculated by dividing the difference in axial thrust coefficient between experimental results and

CFD results by the $\Delta C_t$and then multiplying by 100. The CFD model was therefore validated in case of with J-groove.

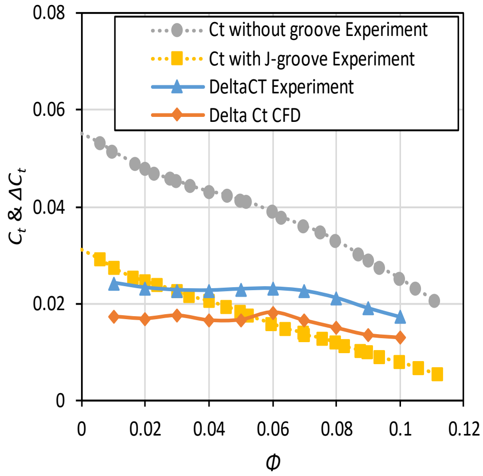


*Fig. 3.8 Axial thrust coefficient and flow coefficient*

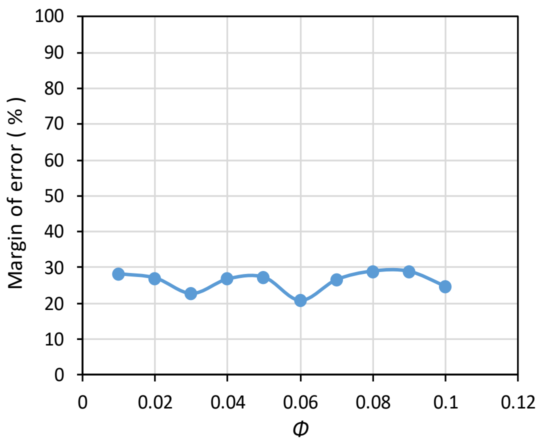


*Fig. 3.9 Margin of error and flow coefficient*

### 3.3 Summary of Chapter 3

For the simple case of the rotor-stator cavity only, the numerical method applied shows good agreement with the experimental data taken from the literature. Finally, the results obtained with the $k$- $\omega$ SST model are closest to the experiments for this type of flow.

To test the dependence of the solution on the mesh size, meshes with different degrees of purification were generated.

Agreement can be judged as good although numerical simulation results tend to be over-predictive compared to measured values in some points.

# Chapter 4

# Effect of J-groove on the flow in various gap without through-flow

# Chapter 4: Effect of J-groove on the flow in various gap without through-flow

In this chapter, the effect of J-groove parameters on 3 types of flow without through-flow will be shown. The 3 types of gaps used for simulation are narrow, intermediate, and relatively large in 4.1, 4.2 and 4.3, respectively. Here, the “narrow gap” is indicated for the case of completely interfered gap, where the “large gap” is for the case of completely non-interfered gap. And the “intermediate gap” is mixture of interfered and non-interfered, that is, in some area the boundary layers are interfered but in other area 2 layers are not interfered. In each section, the effect of parameters of J-grooves on the flow is presented.

## 4.1 Effect of J-groove on the flow in narrow gap

### 4.1.1 Objectives

This section aims to reveal the effect of radial J-groove radial groove on flow in case of narrow gap. First, the fundamental properties of this flow in the absence of a groove have been studied theoretically and experimentally before. Second, the effect of the J-groove and its parameters on the pressure distribution will be compared with the no-groove case. The effect of different design parameters was observed in this section.  J-groove is mounted on the casing wall with the original design of the J-Groove had $n$ = 9, $D$ = 0.0067 (i.e., $d$ = 1 mm), $L$ = 0.4 (i.e., $l$ = 60 mm) and $W$ = 0.1333 (i.e., $w$ = 20 mm). The list of J-Groove models with variation of design parameters is listed in Table 4-1. The number of J-Groove varies from 3 to 12. The depth of J-Groove varies from 0.5 mm to 2 mm. The length of J-Groove is varied from 20 mm to 100 mm. The J-groove depth, length and width varies according to the outer diameter of the disk. The pressure distribution along the radial direction is a good and important indicator of the effect of J-groove. The graphs of the dimensionless radius ratio $R$ and the pressure coefficient $Cp$ show the effect of the groove shape. The results show that radial grooves in the casing wall suggest that this superior effect of J-groove is due to main reasons: one is a significant decrease in tangential velocities due to the mixing of the main and groove flows and the other is an increase in radial velocity due to reverse flow.

*Table 4-1 Parameter of J-groove in narrow gap*

| Type | *n* (number of groove) | *d* (depth) mm | *l* (length) mm | *w* (width) mm |
|---|---|---|---|---|
| I.0 | 0 | 0 | 0 | 0 |
| I.1 | 3 | 1 | 60 | 20 |
| I.2 | 6 | 1 | 60 | 20 |
| I.3 | 9 | 1 | 60 | 20 |
| I.4 | 12 | 1 | 60 | 20 |
| II.1 | 9 | 0.5 | 60 | 20 |
| II.2 | 9 | 1.5 | 60 | 20 |
| II.3 | 9 | 2 | 60 | 20 |
| III.1 | 9 | 1 | 20 | 20 |
| III.2 | 9 | 1 | 40 | 20 |
| III.3 | 9 | 1 | 80 | 20 |
| III.4 | 9 | 1 | 100 | 20 |
| IV.1 | 9 | 1 | 60 | 5 |
| IV.2 | 9 | 1 | 60 | 10 |
| IV.3 | 9 | 1 | 60 | 15 |
| IV.4 | 9 | 1 | 60 | 25 |
| IV.5 | 9 | 1 | 60 | 30 |
| IV.6 | 9 | 1 | 60 | 35 |
| IV.7 | 9 | 1 | 60 | 40 |
| IV.8 | 9 | 1 | 60 | 45 |

### 4.1.2 Results and Discussions

#### 4.1.2.1 Effect of the number of J-groove

To examine the effect of the number of J-groove, we change the angular of the sector of computing area on the number of J-Groove. Therefore, for 3 J-groove a $120^0$ sector is used, for 6 J-groove a $60^0$ sector for 9 J-groove a $40^0$ sector and for 12 J-groove a $30^0$ sector. The effect of number of grooves is shown in Fig. 4.1. with the other groove geometry parameters are typical constant value (i.e., $d = 1$ mm; $l$ = 60 mm and $w$ = 20 mm, corresponding to dimensionless parameters $D = d/r_2 = 0.0067$ ; $L = l/r_2 = 0.4$ and $W = w/r_2 = 0.1333$ respectively). An increase in the number of grooves makes the pressure distribution flat. Fig. 4.2 illustrates the streamlines from R = 0.5 to R = 1 near the casing wall of grooves side for 4 different numbers

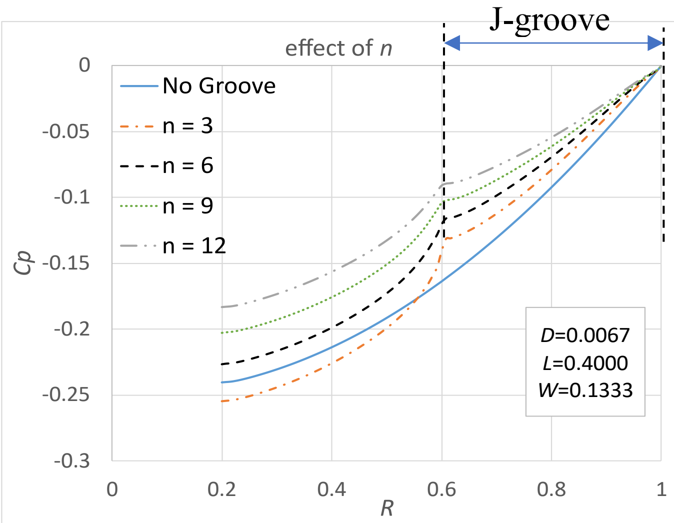


*Fig. 4.1 comparison of pressure distribution by n (S=0.005)*

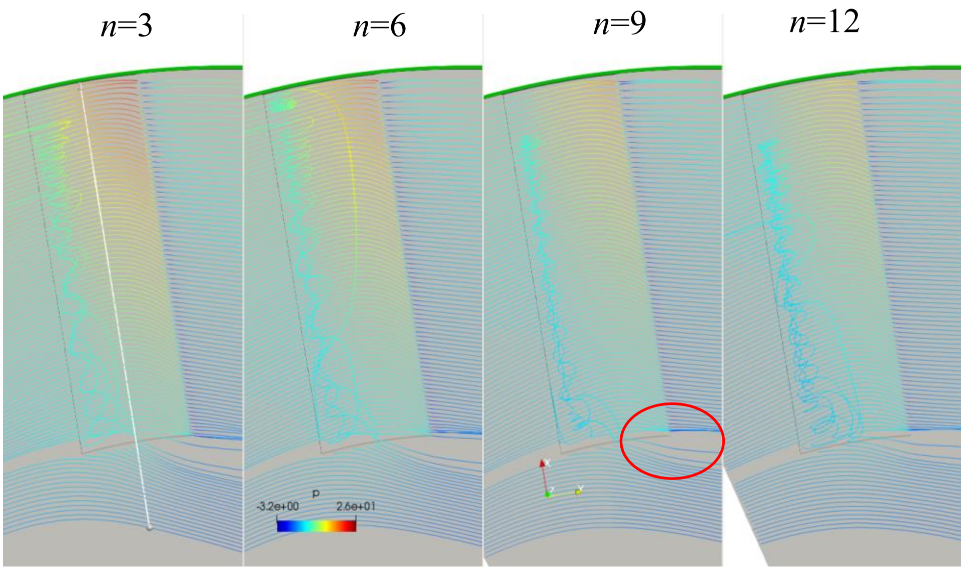


*Fig. 4.2 streamline for different number of grooves*

of J-grooves. According to the CFD visualization of the flow, as shown in Fig. 4.2, the flows are distorted at the tip of the groove. Increasing in number, the flow is distorted decreasingly. Following this when n becomes larger, hydraulic loss becomes large, and the pressure drops dramatically.

#### 4.1.2.2 Effect of the depth of J-groove

In Fig. 4.3. and Fig. 4.4., the effect of depth of the groove is shown. Four cases were analyzed for dimensionless width ratio $W$ = 0.1333. Remaining the other groove geometry constant, when the depth of the groove is increased from dimensionless depth ratio $D$ = 0.0033 to $D$ = 0.0133, the pressure increased significantly. But when $D$ = 0.0033 (i.e., $d$ = 0.5 mm), the pressure decreased in comparison with the case without the groove, when $D$ = 0.0033, only the hydraulic loss becomes larger in these cases in comparison with the case without groove. This explains why the pressure is lower near the hub when $D$ = 0.0033. Consequently, too shallow grooves increase axial thrust.

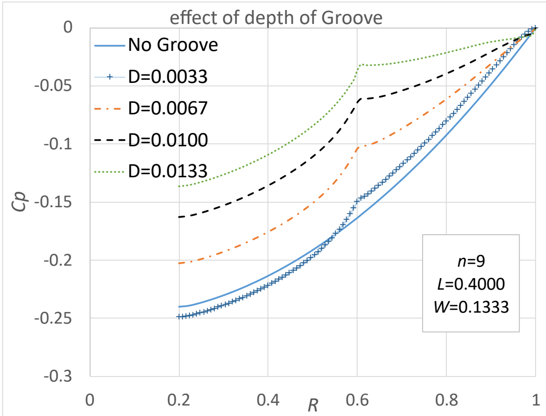


*Fig. 4.3 pressure distribution by D (S=0.005)*

#### 4.1.2.3 Effect of the length of J-groove

Effect of length of groove is shown in Fig. 4.5. for different length ratios $L = l/r_2$. Increasing the length of the groove not only decreases the peak pressure but also decreases the pressure difference across the rotating disk and makes the axial thrust lower. When the grooves have $L$ = 0.1333 (i.e., $l$ = 20 mm), the pressure decreased in comparison with the case without the groove.

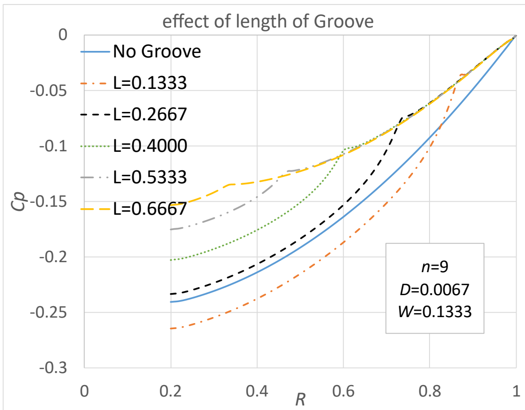


*Fig. 4.4 pressure distribution by L (S=0.005)*

### 4.1.2.4 Effect of the width of J-groove

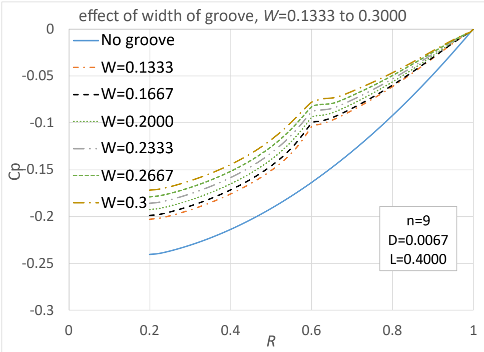


*Fig. 4.5 pressure distribution by W, W=0.1333 to 0.2333 (S=0.005)*

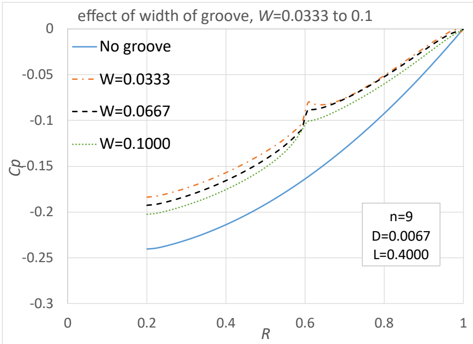


*Fig. 4.6 pressure distribution by W, W=0.0333 to 0.1 (S=0.005)*

The effect of different widths of J-grooves is shown in Fig. 4.5. and Fig. 4.6. Six cases were analyzed with $W = 0.1333$ to $W = 0.3$, corresponding to $w = 20$ mm to $w = 45$ mm wide of J-groove and 3 cases with $W = 0.0333$ to $W = 0.1$, corresponding to $w = 5$ mm to $w = 15$ mm. As shown in Fig. 4.6., remaining the other groove geometry constant, when the width of groove is increased from dimensionless width ratio $W = 0.0333$ to $W = 0.1$, the pressure is reduced but not much. Also, in Fig. 4.5. can be noticed that when $W = 0.1333$ to $W = 0.3$, the pressure increases. However, greater values of the width of the groove will lead to problems related to fabrication, especially for regions with a lower radius of the gap.

### 4.1.2.5 Velocity distribution

According to the CFD visualization of the flow in the groove above, the flow rotated by the rotating wall goes into the groove area.

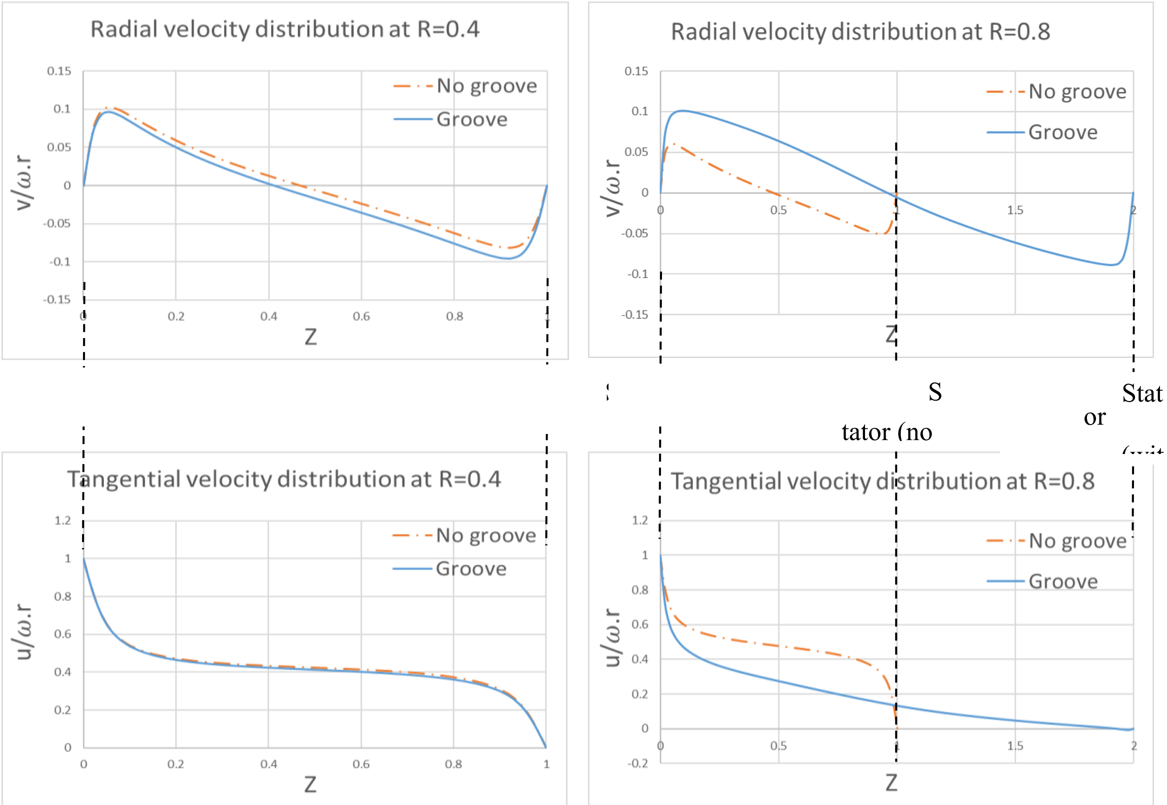


velocity profile, R=0.4 velocity profile, R=0.8

*Fig. 4.7 velocity profile*

Velocity distributions at the center of the sketch between rotor wall and stator wall for $R$ = 0.4 and $R$ = 0.8 are shown in Fig. 4.10. Both the tangential and radial velocity components are plotted in a dimensionless form. The radial velocity at these locations shows evidence of radial inflow and recirculation radially outward back up the stator in both cases. For $R$ = 0.4 there are tangential velocity boundary layers on both walls but for $R$ = 0.8, in the case of J-groove, there is not boundary layer on the stator and only on the rotor. By providing J-groove, the tangential velocity was significantly reduced and become distorted. Furthermore, the radial velocity increase near to the walls in the case of J-groove than that of no groove which is due to the decrease in swirl and reversed flow. They are the effect of J-grooves.

### 4.2 Effect of J-groove on the flow in intermediate gap

#### 4.2.1 Objectives

This section presents the effect of the J-groove on the flow in the intermediate gap ($S$ = 0.0113). The original design of the J-groove had $n$ = 9, $D$ = 0.0133 (i.e., $d$ = 2 mm), $L$ = 0.4 (i.e., $l$ = 60 mm) and $W$ = 0.1333 (i.e., $w$ = 20 mm). The list of J-Groove models with variation of design parameters is listed in Table 4-2. The number of J-Groove varies from 3 to 12. The depth of J-Groove varies from 0.5 mm to 2.5 mm. The length of J-Groove is varied from 20 mm to 100 mm. The graphs of the dimensionless radius ratio $R$ and the pressure coefficient $Cp$ show the influence of the groove shape. The results show that radial grooves in the casing wall suggest that this superior effect of J-groove is due to main reasons: one is a significant decrease in tangential velocities due to the mixing of the main and groove flows and the other is an increase in radial velocity due to reverse flow.

*Table 4-2 Parameter of J-groove in intermediate gap*

| Type | *n* (number of groove) | *d* (depth) mm | *l* (length) mm | *w* (width) mm |
|---|---|---|---|---|
| I.0 | 0 | 0 | 0 | 0 |
| I.1 | 3 | 2 | 60 | 20 |
| I.2 | 6 | 2 | 60 | 20 |
| I.3 | 9 | 2 | 60 | 20 |
| I.4 | 12 | 2 | 60 | 20 |
| II.1 | 9 | 0.5 | 60 | 20 |
| II.2 | 9 | 1 | 60 | 20 |
| II.3 | 9 | 1.5 | 60 | 20 |
| III.1 | 9 | 2 | 20 | 20 |
| III.2 | 9 | 2 | 40 | 20 |
| III.3 | 9 | 2 | 80 | 20 |
| III.4 | 9 | 2 | 100 | 20 |
| IV.1 | 9 | 2 | 60 | 5 |
| IV.2 | 9 | 2 | 60 | 10 |
| IV.3 | 9 | 2 | 60 | 15 |
| IV.4 | 9 | 2 | 60 | 25 |
| IV.5 | 9 | 2 | 60 | 30 |
| IV.6 | 9 | 2 | 60 | 35 |
| IV.7 | 9 | 2 | 60 | 40 |
| IV.8 | 9 | 2 | 60 | 45 |

### 4.2.2 Results and Discussions

#### 4.2.2.1 Effect of the number of J-groove

In Figure 4.8, the effect of the number of grooves shown. Keeping the other groove geometry unchanged, as the number of grooves increases, the pressure distribution is flattened. Increase the number, increase the total volume of the groove and thus the groove current absorbs more angular momentum.

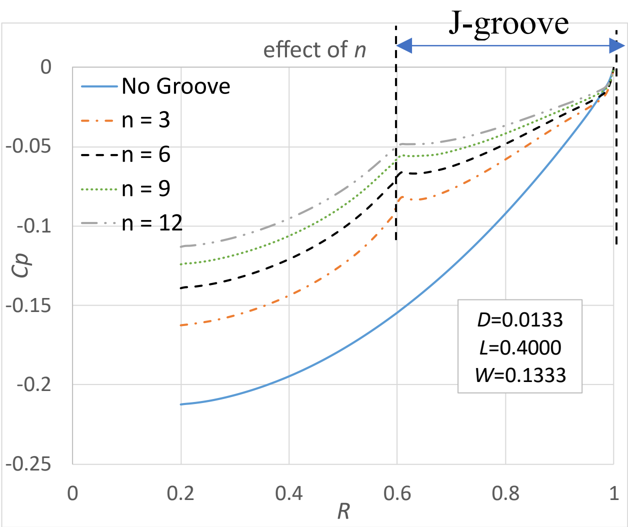


*Fig. 4.8 comparison of pressure distribution by n (S=0.0113)*

#### 4.2.2.2 Effect of the depth of J-groove

In Figure 4.9, the influence of groove depth is shown. Keeping the other groove geometry, when increasing the groove depth from $D$ = 0.0667 to $D$ = 0.0167, the pressure increases significantly. It can be remarked here that the grooves have $D$ = 0.0033 (i.e., $d$ = 0.5 mm), the pressure decreased in comparison with the case without the groove.

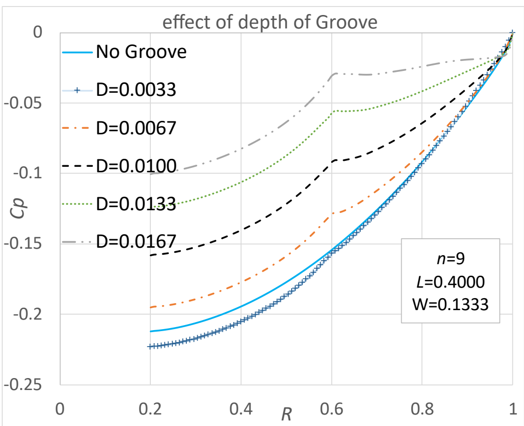


*Fig. 4.9 comparison of pressure distribution by D (S=0.0113)*

#### 4.2.2.3 Effect of the length of J-groove

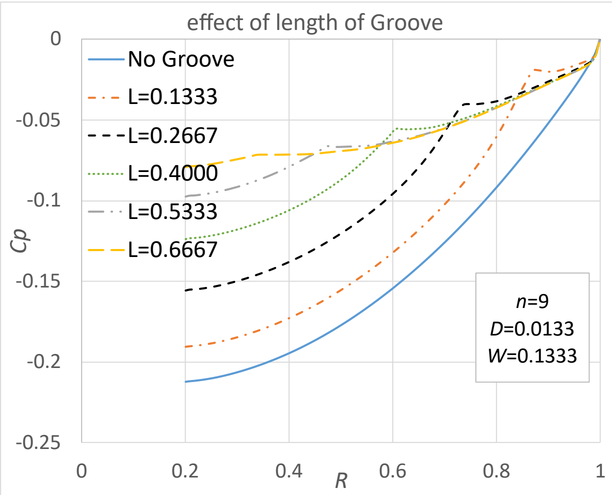


*Fig. 4.10 comparison of pressure distribution by L (S=0.0113)*

The influence of groove length is shown in Figure 4.10. It is also seen here that as the groove length is increased, the pressure also increases as before even if when the groove is very short.

#### 4.2.2.4 Effect of the width of J-groove

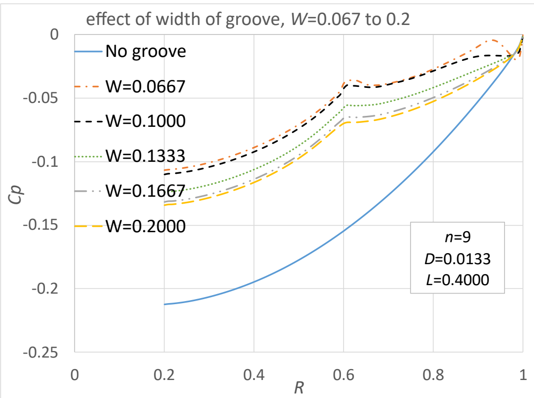


*Fig. 4.12 pressure distribution by W, W=0.0667 to 0.2*

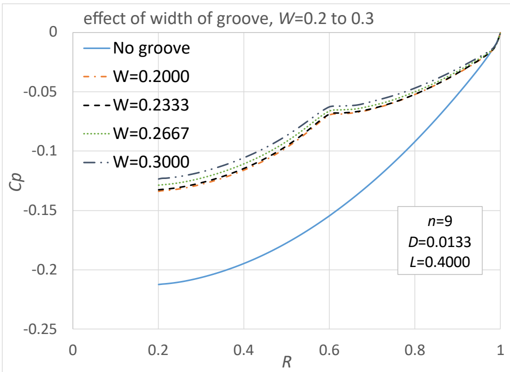


*Fig. 4.11 pressure distribution by W, W=0.033 to 0.233*

The effects of different widths of the J-groove are shown in Fig. 4.11. and Fig. 4.12, with $W = 0.0667$ to $W = 0.\ 3$, corresponding to the width of the groove $w$ = 10 mm to $w$ = 45 mm. As shown in Fig. 4.11., remaining the other groove geometry constant, when the width of groove is increased $W = 0.2$ to $W = 0.3$, the

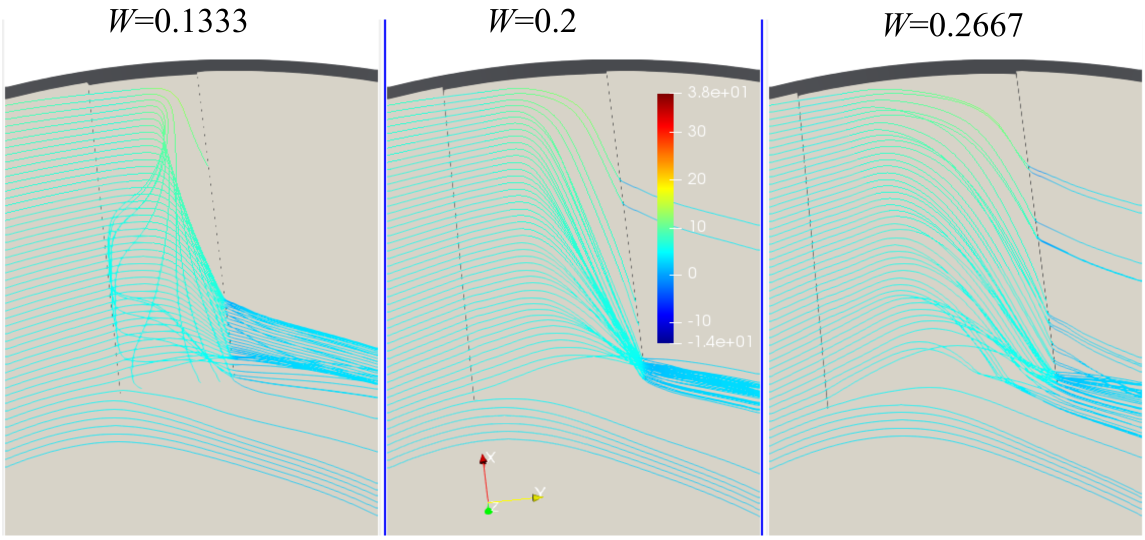

*Fig. 4.13 streamline for W=0.1333, W=0.2 and W=0.2667*

pressure is flattened but not much. However, greater values of the width of the groove will lead to problems related to fabrication, especially for regions with a lower radius of the gap. Also, in Fig. 4.12. can be noticed that when $W = 0.0667$ to $W = 0.2$, the pressure reduces with an increase in the width of the groove. As shown in Fig. 4.13, in typical cases of $W = 0.1333$ and $W = 0.2667$, the flow is bending to the hub region, although the flow is quite smooth. With the flow pattern in case $W = 0.1333$, the pressure becomes flat, in which J-grooves make the rotational (tangential) speed low. The radial flow from the outer to inner causes such reduction of tangential velocity, as the result of transferred fluid with low angular momentum along the groove. In contrast, in the case of the groove width ratio $W = 0.2$, the flow is greatly distorted at the tip of the groove, resulting in an increase in hydraulic loss. This leads to a decrease in pressure remarkably.

### 4.3 Effect of J-groove on the flow in relatively large gap

#### 4.3.1 Objectives

This section is aimed to reveal the influence of the J-groove on the flow in the case of large gap. The influence of the J-groove and its parameters on the pressure distribution will be simulated to compare with the case without the groove. The influence of various design parameters has been observed in this section. The original design of the J-Groove had $n = 9$, $D = 0.0133$ (i.e, $d = 2$ mm),

$L$ = 0.4 (i.e, $l$ = 60 mm) and $W$ = 0.1333 (i.e, $w$ = 20 mm). The list of J-Groove models with variation of design parameters is listed in Table 4-3. The number of J-Groove varies from 3 to 12. The depth of the J-Groove varies from 0.5 mm to 2 mm. The length of J-Groove is varied from 20 mm to 100 mm. The depth, length and width of the J-groove varies according to the outer diameter of the disk.

*Table 4-3 Parameter of J-groove in large gap*

| Type | $n$ (number of groove) | $d$ (depth) mm | $l$ (length) mm | $w$ (width) mm |
|---|---|---|---|---|
| I.0 | 0 | 0 | 0 | 0 |
| I.1 | 3 | 2 | 60 | 20 |
| I.2 | 6 | 2 | 60 | 20 |
| I.3 | 9 | 2 | 60 | 20 |
| I.4 | 12 | 2 | 60 | 20 |
| II.1 | 9 | 0.5 | 60 | 20 |
| II.2 | 9 | 1 | 60 | 20 |
| II.3 | 9 | 1.5 | 60 | 20 |
| III.1 | 9 | 2 | 20 | 20 |
| III.2 | 9 | 2 | 40 | 20 |
| III.3 | 9 | 2 | 80 | 20 |
| III.4 | 9 | 2 | 100 | 20 |
| IV.1 | 9 | 2 | 60 | 5 |
| IV.2 | 9 | 2 | 60 | 10 |
| IV.3 | 9 | 2 | 60 | 15 |
| IV.4 | 9 | 2 | 60 | 25 |
| IV.5 | 9 | 2 | 60 | 30 |
| IV.6 | 9 | 2 | 60 | 35 |
| IV.7 | 9 | 2 | 60 | 40 |
| IV.8 | 9 | 2 | 60 | 45 |

### 4.3.2 Results and Discussions

#### 4.3.2.1 Effect of the number of J-groove

The characteristic curve illustrated in Fig. 4.14 shows the change of the number of J-grooves while the other parameters are kept constant. With increasing the number of grooves, the pressure distribution is flattened from *n* = 3 to *n* = 12 due to increase the total volume of the groove and thus the groove current absorbs more angular momentum.

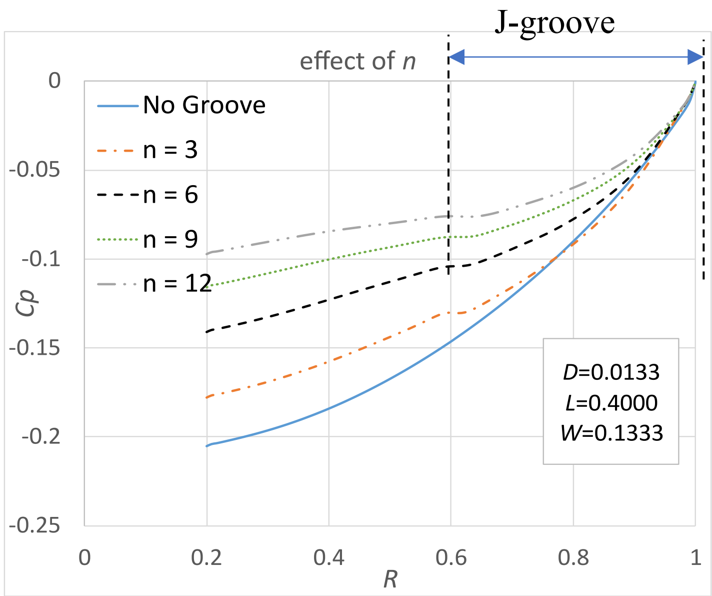


*Fig. 4.14 comparison of pressure distribution by n (S=0.0556)*

#### 4.3.2.2 Effect of the depth of J-groove

Figure 4.15. shows the effect of groove depth on the case of large gap. Unlike the previous two cases of narrow gap and intermediate gap, in this case, grooves with a depth of only 0.5 mm in the casing wall can also show the effect of the J-groove.

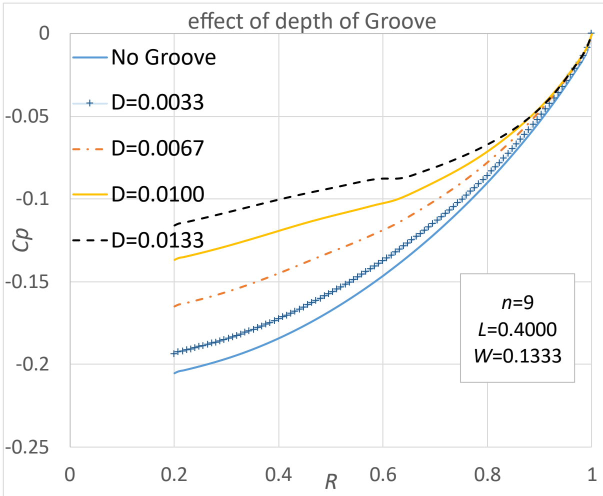


*Fig. 4.15 comparison of pressure distribution by D (S=0.0556)*

#### 4.3.2.3 Effect of the length of J-groove

The influence of groove length is shown in Fig. 4.16 for different length ratios $L = l/r_2$ from 0.0133 to 0.6667. Increasing the length of the groove decreases the pressure differential across the rotating disk and leads to longitudinal thrust axis is lower than in the previous two cases.

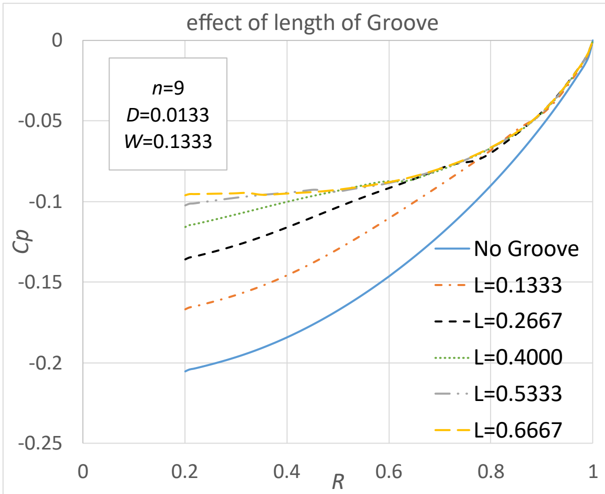


*Fig. 4.16 comparison of pressure distribution by L (S=0.0556)*

#### 4.3.2.4 Effect of the width of J-groove

Figure 4.17 and Fig. 4.18 shows the influence of the J-Groove width on the pressure coefficient distribution. The increase in the J-Groove width has a limited effect on the pressure coefficient distribution, i.e., in this case, when the $W = 0.0667$ to $W = 0.2$, the pressure distribution is almost the same. And $W = 0.2$ to $W = 0.3$, the pressure distribution is flattened but no change much as shown in Fig. 4.18.

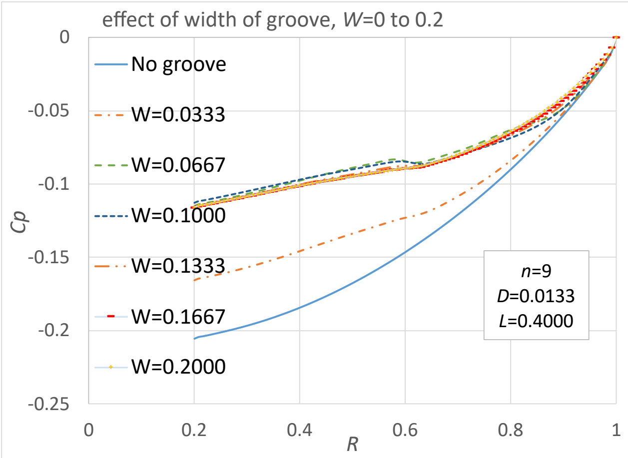


*Fig. 4.17 comparison of pressure distribution by W, W =0 to 0.2 (S=0.0556)*

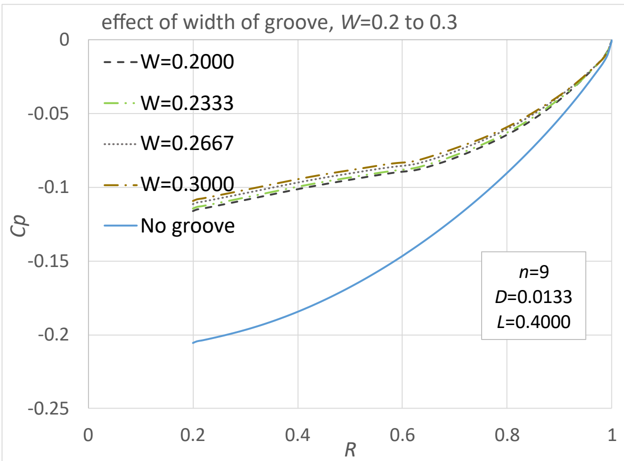


*Fig. 4.18 comparison of pressure distribution by W, W =0.2 to 0.3 (S=0.0556)*

### 4.4 Summary of Chapter 4

In this chapter, the influence of the J-groove and its parameters on the pressure distribution has been simulated to compare with the case without the groove. The pressure distribution along the radial direction is a good and important indicator of J-groove performance. The graphs of the dimensionless radius ratio *R* and the pressure coefficient *Cp* represent the influence of the J-groove. Significant decrease in tangential velocity due to mixing of main flow and groove flow, and significant increase in radial velocity due to reverse flow.

The difference in pressure between the outer and inner radius increases as the number, depth, and length of the J-groove increases in almost cases. There is a critical value for the J-Groove parameters. The pressure distribution indicated that the J-Groove depth should be greater than the critical value in case of without through-flow for narrow and intermediate gap. However, in the case of increasing the width of the J-groove, the pressure decreases when the ratio of the groove width to the outside radius *W* is less than 0.2 (0.1333) and increases when *W* is more than 0.2 (0.1333) in intermediate gap (narrow gap). In addition, when the coefficient depth of the J-groove $D$ = 0.0033, the effect of the J-groove is not improved due to the increased hydraulic loss.

# Chapter 5

# Effect of J-groove on the flow in various gap with through-flow

## Chapter 5: Effect of J-groove on the flow in various gap with through-flow

### 5.1 Overview the case of inward through-flow

In principle, the radial pressure distribution is determined from the rotation of the fluid in the gap and the leakage flow rate. An axial inflow is now supplied to the cavity. The coefficient flow rate $C_q = \left( Q / 2\pi r_2^3 \omega \right) Re^{1/5}$ in each gap between two concentric disks is studied in this section. In chapter 4, $C_q$= 0 case is studied. With an increased flow rate, the rotational speed of the fluid increases as shown in Fig. 5.1. This is consistent with the conservation of angular momentum of the radial flow. In this figure, the tangential velocity is dimensionless and equal $\frac{u}{\omega . r}$, where *u* is plotted on the line at mid-cavity. In case of $C_q = 0$, the tangential velocity in the core is almost equal to 0.5 of the disk speed and that non-dimensional *u* is once reduced and suddenly up near *r* = 0.2, because of corner effect, as we can see in Fig. 5.2 and Fig. 5.3.

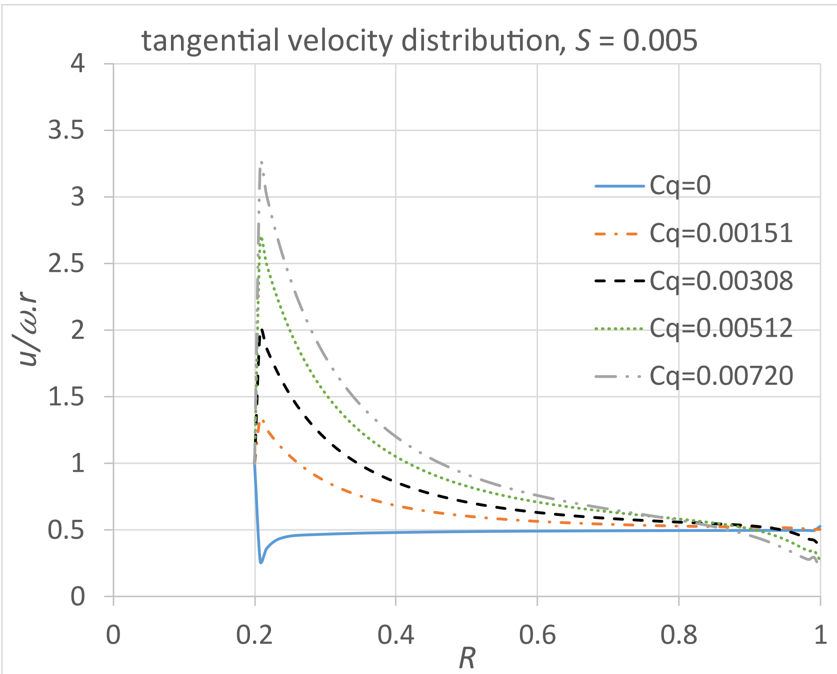


*Fig. 5.1 comparison of tangential velocity for S = 0.005*

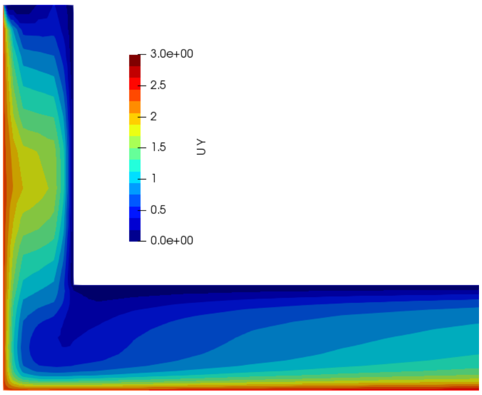


*Fig. 5.3 contour of the tangential velocity*

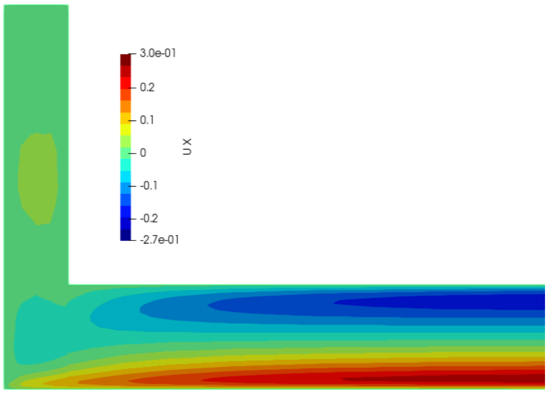


*Fig. 5.2 contour of the radial velocity*

Velocity profiles for dimensionless tangential and radial velocities at $R$ = 0.8 are given in Figures 5.4 and 5.5, respectively. With increasing through-flow the radial velocity forward to center is increased. The flow structure is divided into two layers: a centrifugal boundary layer on a rotating disc and a radial boundary layer on a stationary disc divided by a rotating core and a near-zero radial component. The tangential velocity in the core increases due to superimposed radial currents. The two boundary layers are both radial for stronger radial currents, causing the core to rotate faster than the rotor.

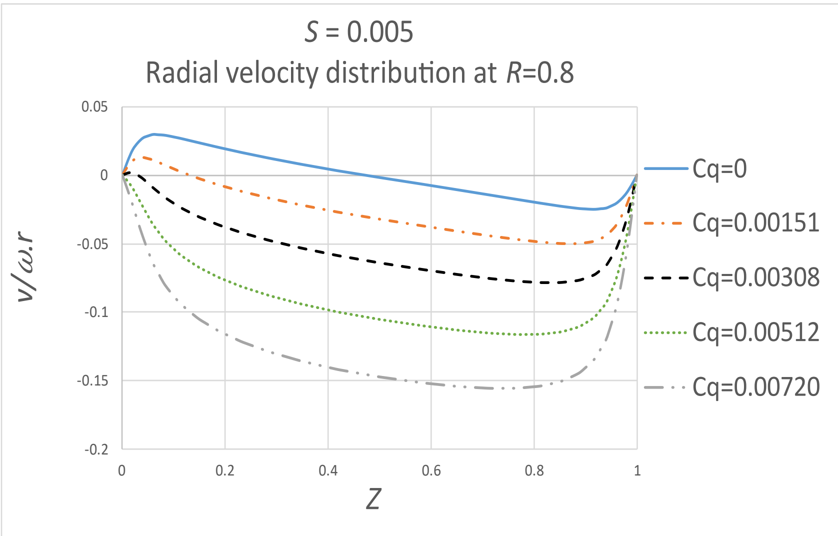


*Fig. 5.4 radial velocity distribution at R = 0.8*

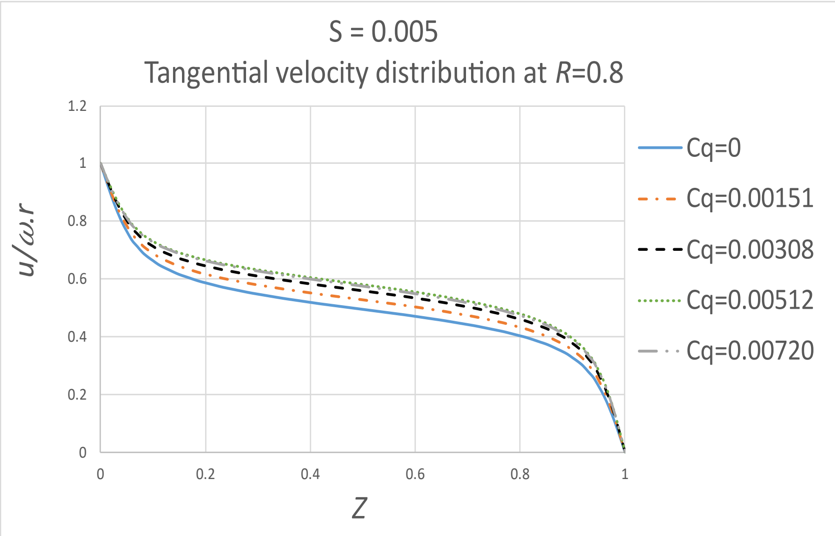


*Fig. 5.5 tangential velocity distribution at R = 0.8*

In the case of weak flow, the peripheral flow has the same properties as in the case of no flow. However, when a strong flow rate is present, the flow in the boundary layer near the rotating disk becomes radial, and the core rotates faster than the rotating disk. In a particular analysis, only one parameter (flow rate coefficients) was changed to study its effect. The selection of these geometrical parameters is consistent with the work done in the previous chapter.

## 5.2 Effect of J-groove on the flow in narrow gap

### 5.2.1 Objectives

In this section, the effect of J-groove on the radial pressure distribution on the flow in narrow gap with through-flow will be presented. The parameters of J-groove are taken from the parameters in Table 4-1, with flow rate coefficient $Cq$ = 0.0151. Referencing these figures, the same behavior is encountered.

### 5.2.2 Results and Discussions

To predict the optimal J-groove size, the influence of the J-groove size on the radial pressure distribution was investigated using the groove samples shown in Table 4-1. Some characteristic curves are illustrated in Fig. 5.6 to Fig. 5.9 for the variation of the J-groove number $n$, depth $D$, length $L$ and width $W$.

When the J-groove is installed on the casing wall, its effect is evident in the radial pressure distribution. But from Figure 5.6 it is shown that, when increasing the number $n$ of the grooves in the flow-through case, the pressure change between these cases is not obvious. Figure 5.7 shows that, in the case of through-flow, even though the groove depth is very shallow ($D = 0.0033$), the pressure distribution is flatten. This is different from the case without through-flow in section (4.1.2.2). The influence of groove length is shown in Figure 5.8. It is also found here that when the groove length is increased, the pressure is also flattened, but the effect is not improved due to the shorter groove ($L = 0.1333$). The effects of different widths of the J-groove are shown in Figure 5.9 and Figure 5.10, with a dimensionless width ratio $W = 0.0333$ to $W = 0.3$. From Figure 5.10, it can be observed that when $W = 0.0333$ to $W = 0.1$, the pressure decreases as the width of the groove increases, conversely, as shown in Figure 5.9, when increasing the width of the groove from $W = 0.1333$ to $W = 0.3$, pressure is flattened.

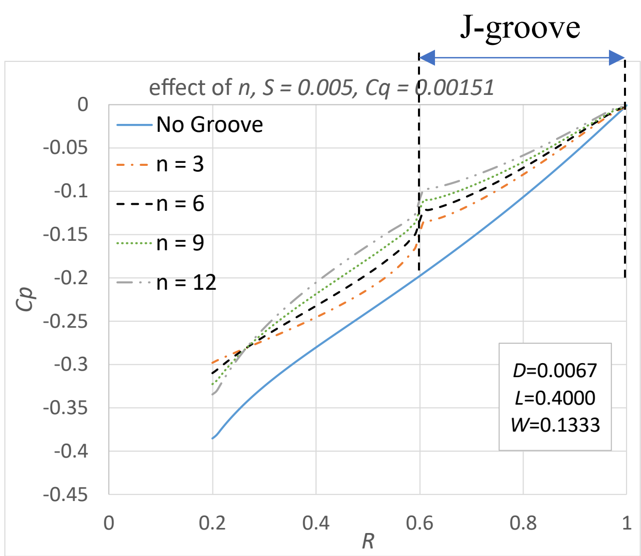


*Fig. 5.6 pressure distribution by n (Cq = 0.00151)*

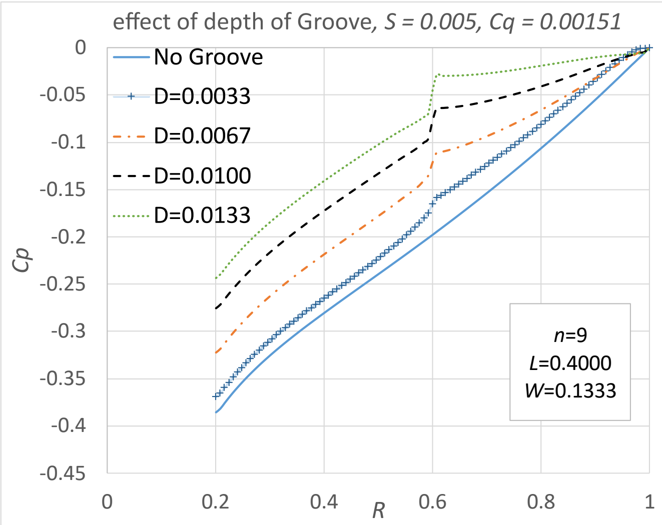


*Fig. 5.7 pressure distribution by D (Cq = 0.00151)*

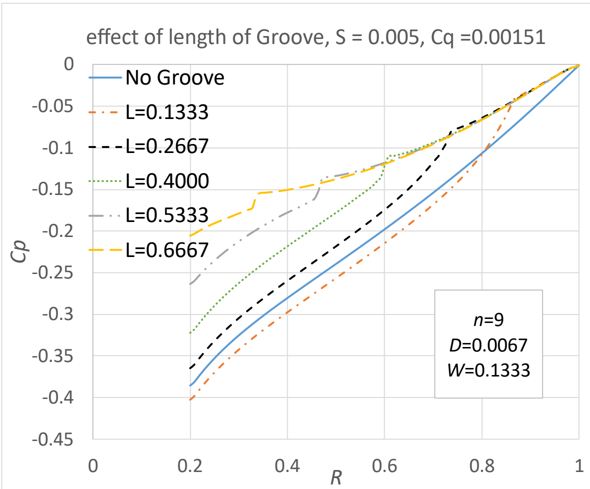


*Fig. 5.8 pressure distribution by L (Cq = 0.00151)*

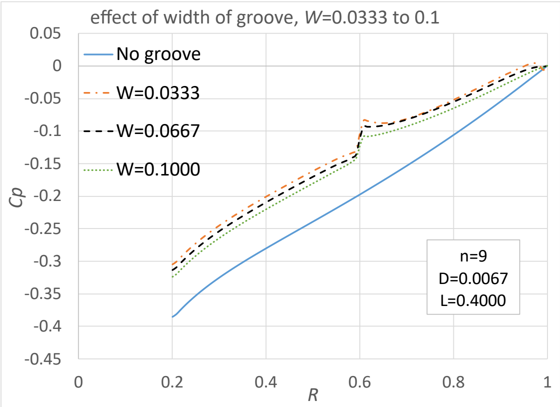


*Fig. 5.10 pressure distribution by W, W=0.0333 to 0.1333 (Cq = 0.00151)*

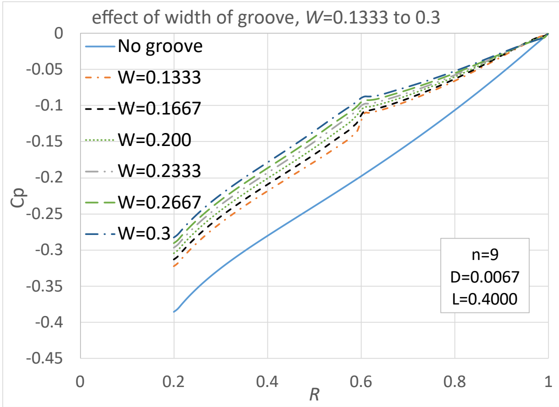


*Fig. 5.9 pressure distribution by W, W=0.1333 to 0.3 (Cq = 0.00151)*

## 5.3 Effect of J-groove on the flow in intermediate gap

### 5.3.1 Objectives

In this section, the effect of the J-groove on the radial pressure distribution on the flow in the intermediate gap ($S$ = 0.0113) with the flow through will be presented. The parameters of the J-groove are taken according to the same parameters in Table 4-2 in the absence of flow (section 4.2), with a flow rate coefficient $Cq$ = 0.0149.

### 5.3.2 Results and Discussions

It was realized that groove geometry has strong effect on the pressure distribution. Increase in number, depth, and length, of J-groove, the difference in pressure between the outer and inner radius decrease. Shallow and short grooves are effective.

From Fig. 5.15, it can be observed that when $W$ = 0.0667 to $W$ = 0.2, the pressure decreases as the width of the groove increases, conversely, as shown in Figure 5.14, when increasing the width of the groove from $W$ = 0.2 to $W$ = 0.3, the pressure distribution is flattened but not much.

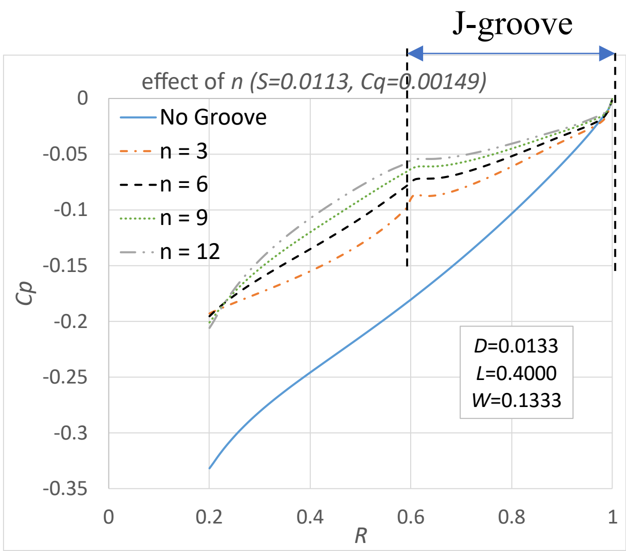


*Fig. 5.11 pressure distribution by n (Cq=0.00149)*

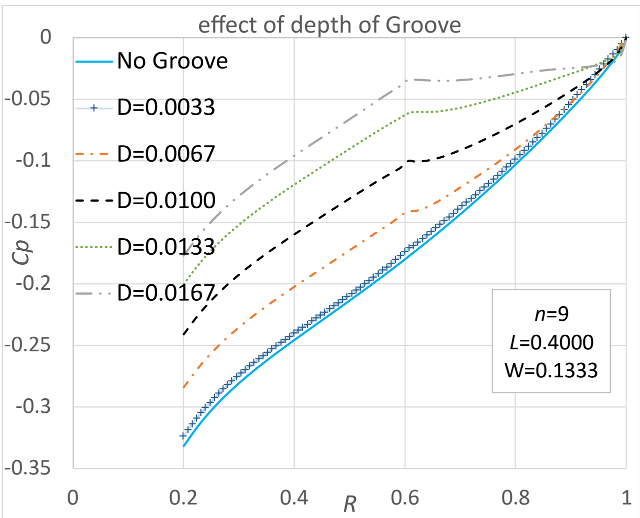


*Fig. 5.12 pressure distribution by D (Cq=0.00149)*

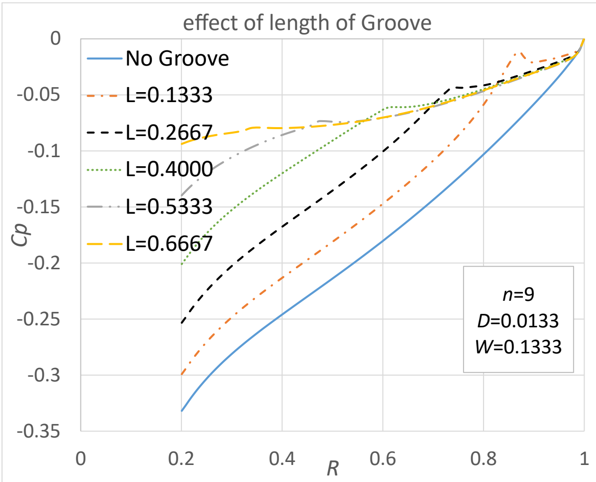


*Fig. 5.13 pressure distribution by L (Cq=0.00149)*

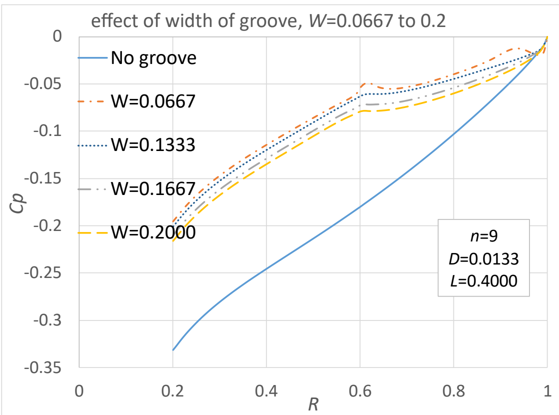


*Fig. 5.15 pressure distribution by W, W=0.0667 to 0.2 (Cq=0.00149)*

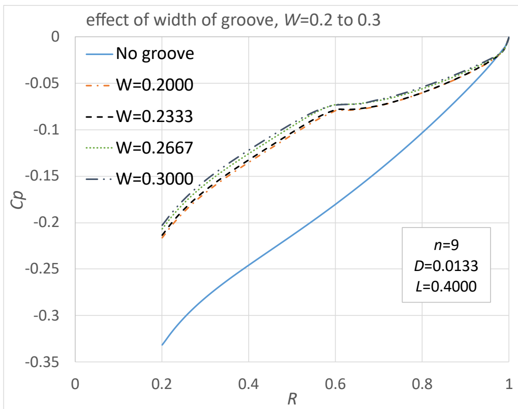


*Fig. 5.14 pressure distribution by W, W=0.2 to 0.3 (Cq=0.00149)*

## 5.4 Effect of J-groove on the flow in large gap

### 5.4.1 Objectives

In this section, the effect of the J-groove on the distribution of radial pressure on the flow in the relatively large gap ($S = 0.0556$) with the through-flow will be presented. The parameters of the J-groove are taken according to the same parameters in Table 4-3 in the absence of flow (section 4.3), with a flow rate coefficient $Cq = 0.0136$.

### 5.4.2 Results and Discussions

Some characteristic curves showing the influence of the J-groove on the flow in large gap are illustrated in Figure 5.14. to Figure 5.17. for the variation of different number of groove *n*, depth *D*, length *L* and width *W*.

Increasing the number of grooves *n*, depth *D* and length *L*, the pressure curve becomes flatter. However, in the case of increasing the width *W* of the groove, when *W* is smaller than or equal to 0.2, the effect of J-groove is almost the same as shown in Figure 5.17.

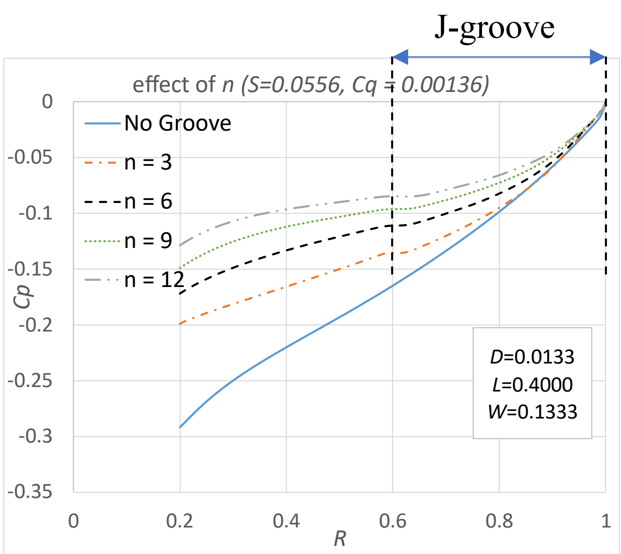


*Fig. 5.16 pressure distribution by n (Cq=0.00136)*

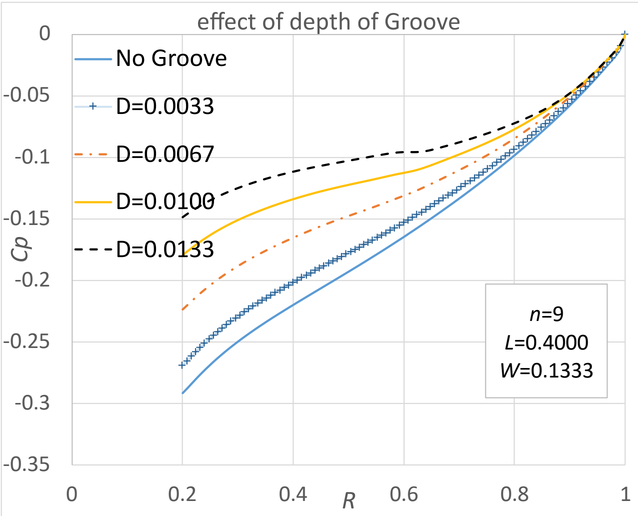


*Fig. 5.17 pressure distribution by D (Cq=0.00136)*

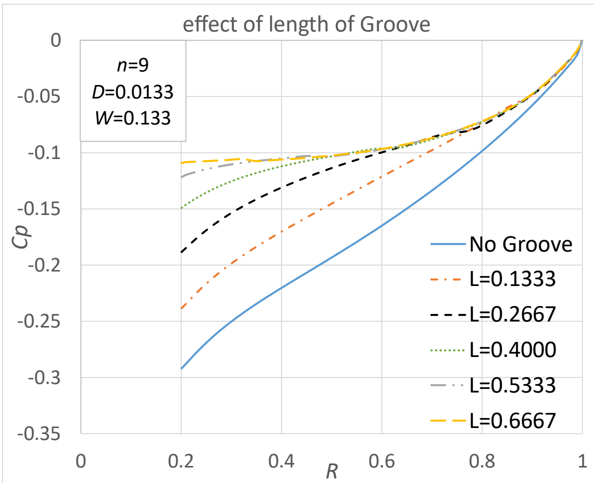


*Fig. 5.18 pressure distribution by L (Cq=0.00136)*

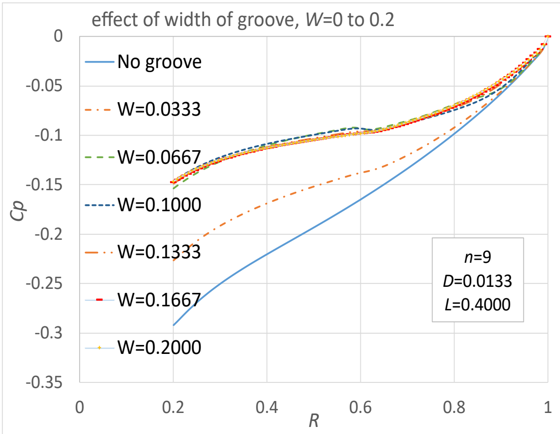


*Fig. 5.19 pressure distribution by W, W =0 to 0.2 (Cq=0.00136)*

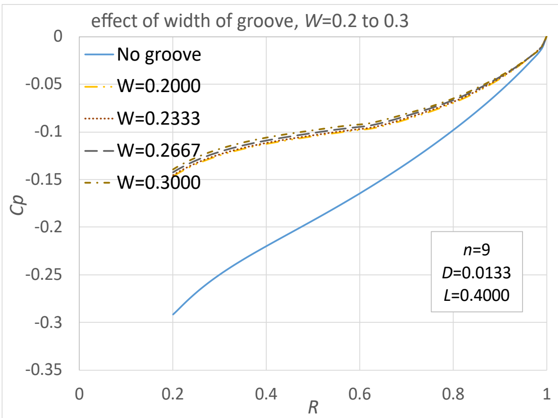


*Fig. 5.20 pressure distribution by W, W =0.2 to 0.3 (Cq=0.00136)*

In comparison with the narrow gap case (Section 5.3.1 above), the tendency of pressure distributions of the intermediate gap is almost the same. With an increase in the number, depth and length of J-groove, the pressure distribution is flattened. Except in the case of the very short length of J-groove, $L$ = 0.1333, in the narrow gap, it does not improve the effect as shown in Fig. 5.8, but in the intermediate gap and in the large gap, that value of length makes the pressure flattened clearly as shown in Fig. 5.13 and Fig. 5.18. The effect of the J-groove width $W$ is presented in Fig. 5.9 and Fig. 5.10 for the narrow gap, in Fig. 5.14 and Fig. 5.15 for the intermediate gap and in Fig. 5.19 and 5.20 for the large gap, while the other parameters of J-groove are constant. It is clear to see that, there is a critical value of J-groove width in each kind of the gap. For the narrow gap, the critical value is equal to 0.12 and for the intermediate and large gap, these critical values are equal to 0.2. The pressure decreases together with increasing the width of J-groove when the width is less than the critical values in the case of narrow and intermediate gaps, then increases when it is greater than those critical values. This was explained in section (4.2.2.4) through the streamlines in the flow field. For the large gap, the J-groove width effect has no significant change when the width is less than critical values.

The pressure gradients in the case of with the leakage flow in narrow gap and intermediate gap in Fig. 5.6 and 5.11 for varies number of J-groove no such sharp in pressure gradients in case of without J-groove, as shown in Fig. 4.1 and 4.8, respectively.

## 5.5 Summary of Chapter 5

A computational study was carried out to investigate the turbulent flow inside the rotor-stator system and to investigate the effect of flow rate. From the analysis of the results, the following conclusions can be drawn. With increasing flow rate, the rotational speed of the fluid increases, and the radial velocity profile becomes more and more radial. The change of the parameters of the J-groove shows its influence on the pressure distribution, as well as the influence on the axial force in the turbomachinery.

# Chapter 6

# The estimation of effect of J-groove with various parameters

# Chapter 6: The estimation of effect of J-groove with various parameters

## 6.1 Overview

To determine the optimal parameters of J-groove, many calculations were performed by the gap sizes and the J-groove dimension. From the radial pressure distribution in chapter 4 and chapter 5, the axial thrust coefficient is determined as following, used to estimate the effect of J-Groove.

$$C_t = \int_{r_1}^{r_2} C_p r dr$$

$$\Delta C_t = C_t - C_{t_{ng}}$$

, where $C_{t_{ng}}$ is the value of axial thrust coefficient in the case of without J-groove and $Cq = 0$.

The dependence of the axial force ratio on the groove parameters is assumed according to the equation below in this study.

Depending on the gap types and with or without through-flow, $\Delta C_t$ independent equations are derived from the results of the CFD simulation. Furthermore, the influence of flow parameters on the flow structure has been studied.

## 6.2 The estimation of effect of J-groove in various gap

From the above formula, we can build graphs of the influence of J-groove parameters on the reduction ratio $\Delta C_t$ of axial force in narrow gap from Fig. 6.1 to Fig. 6.4 for narrow gap without through-flow, Fig. 6.6 to Fig.6.10 for narrow gap with through-flow. Figures 6.12 to Fig. 6.15 and from Fig. 6.17 to Fig. 6.21 show this effect on the flow in intermediate gap without and with through-flow, respectively. The graphs showing the dependence of $\Delta C_t$ on the J-groove parameters in large gap are presented from Fig. 6.23 to Fig. 6.26 for the case without through flow and from Fig. 6.28 to 6.32 for the case with through-flow. All these graphs can be summarized into the prediction equations for narrow gap, intermediate gap, and large gap with the parameters of the J groove *n, D, L, W,* and coefficient flow rate *Cq*.

$\Delta C_t$ is proportional linear to J-groove number, depth, and flow rate coefficient *Cq* for all cases. Only the J-groove width dependency makes a difference. The $\Delta C_t$ value for narrow and intermediate gaps increases initially to a certain value and then decreases after that value, which is 0.12 for narrow gap and 0.2 for intermediate gap. In the large gap, except for the value $W = 0.0333$, when $W < 0.2$, the dependence of the axial force ratio on the groove width is almost unchanged; and when $W > 0.2$, the $\Delta C_t$ decreases with increasing $W$. The comparisons of the CFD and proposed formula of the axial thrust coefficient are plotted in Fig. 6.5 and Fig. 6.11 for the narrow gap, in Fig. 6.16 and 6.22 for the intermediate gap, and in Fig. 6.27 and Fig. 6.33 for the large gap.

### 6.2.1 The estimation of effect of J-groove in narrow gap

From chapter 4 and chapter 5, there is a significant difference between the pressure distribution for each parameter of the J-groove that causes the axial thrust to change. First, the dependence of the axial thrust on each parameter of the J-groove was investigated. Based on those dependencies, a prediction formula was calculated for the dependence of the axial thrust of the J-groove parameters and then do a comparison with those values.

#### 6.2.1.1 In narrow gap without through-flow

From the section (4.1) of this thesis, the results show that J-groove makes the pressure distribution flattened, follow it, the axial thrust can be reduced. They are estimated with the proposed equations with a correlation for $\Delta C_t$ is determined, given in Equation (3.1) and (3.2). The results from these 2 equations are calculated with the CFD results, plotted in Fig. 6.1 to Fig. 6.4. With the increase of number *n,* depth *D* the value of $\Delta C_t$ decrease almost linear and decrease proportion length square. And in case of increase the width of J-groove, the reduction of axial thrust first increase when that value still less than 0.12, then decrease when the value of width is greater than 0.12.

A proposed formula to calculate the axial thrust coefficient $\Delta C_t$ based on the above comments as follow:

$$\Delta Ct = a \times (n) \times (D + b) \times (L^2 + c) \times (|W - 0.12| + d) \qquad (6.1)$$

with $a = -7.1532$; $b = -0.0028$; $c = 0.1358$; $d = 0.176$

Figure 6.5 depicts a graphical comparison of the CFD results and the proposed formula results of the coefficient of axial thrust. The legend on the x-axis represents the cases, whereas the y-axis represents the $\Delta C_t$ value of those cases.

Based on this comparison, the proposed formula's trend is somewhat consistent with the CFD results' trend. However, the two results differ at some points, which can be explained by the unique coefficients a, b, c, and d chosen for the proposed formula (6.1) above.

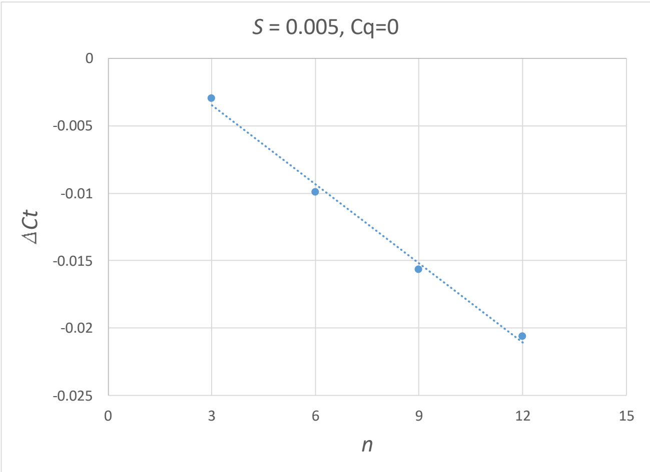


*Fig. 6.1 axial thrust reduction by n*

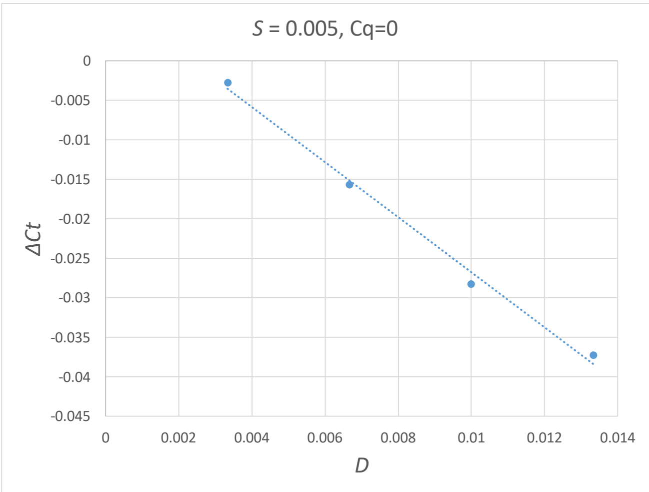


*Fig. 6.2 axial thrust reduction by D*

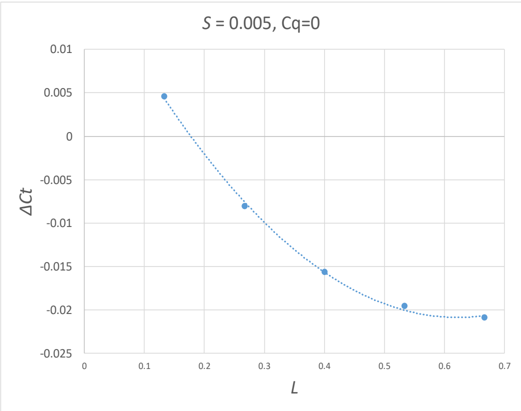


*Fig. 6.4 axial thrust reduction by L*

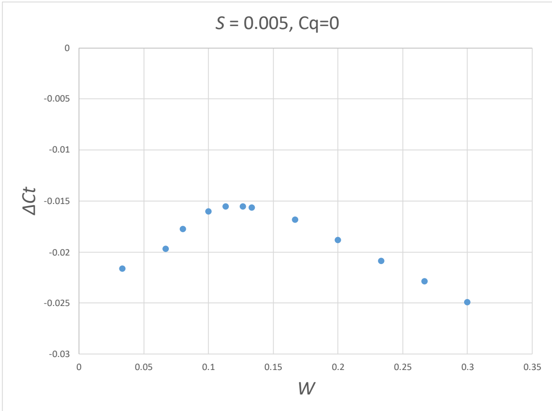


*Fig. 6.3 axial thrust reduction by W*

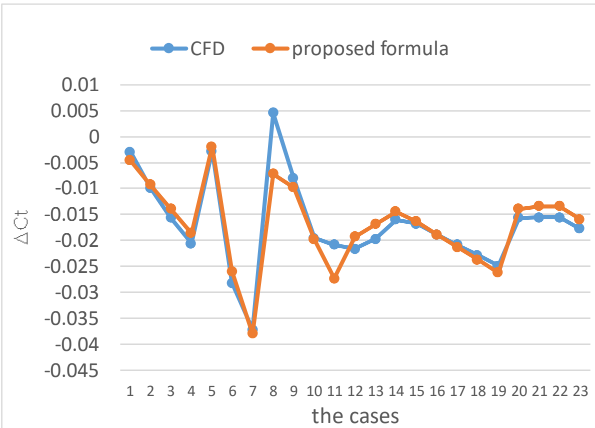


*Fig. 6.5 comparision between CFD and proposed formula (narrow gap, Cq = 0)*

### 6.2.1.2 In narrow gap with through-flow

An axial inflow is now supplied to the narrow gap ($S$ = 0.005), a phenomenon that has been studied in section (5.2). The axial thrust factor $\Delta C_t$ can be calculated and plotted from the pressure distribution of that section in Fig. 6.6 to Fig. 6.10. The $\Delta C_t$ has a linear relationship with number *n*, depth *D*, and flow rate coefficient $Cq$. As $W$ increases, $\Delta C_t$ increases when $W$ is less than 0.12 and decreases when $W$ is greater than 0.12, as shown in Figure 6.9. The following is the expected calculation formula for $\Delta C_t$ based on the preceding statements:

$$\Delta Ct = a \times (n + b) \times (D + c) \times (L^2 + d) \times (|W - 0.12| + e) \times Cq \qquad (6.2)$$

with a = -135.18; b = -4; c = -0.0053; d = -0.072; e = 0.0537.

Follow this formula, the comparison of the CFD results (blue) and proposed formula results (orange) of reduction axial thrust is presented in Fig. 6.11.

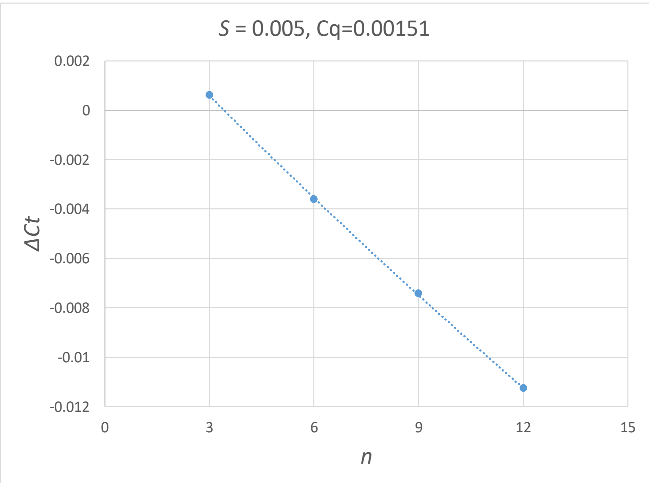


*Fig. 6.6 axial thrust reduction by n*

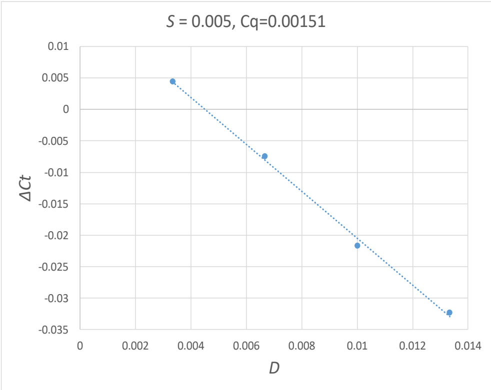


Fig. 6.7 axial thrust reduction by D

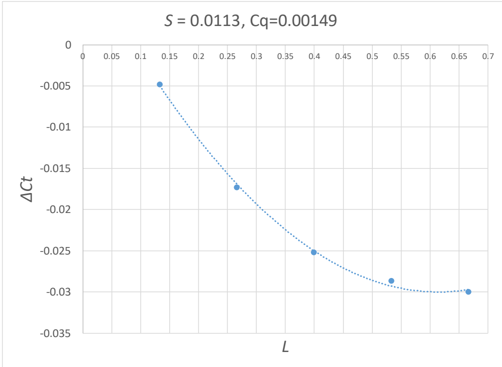


Fig. 6.8 axial thrust reduction by L

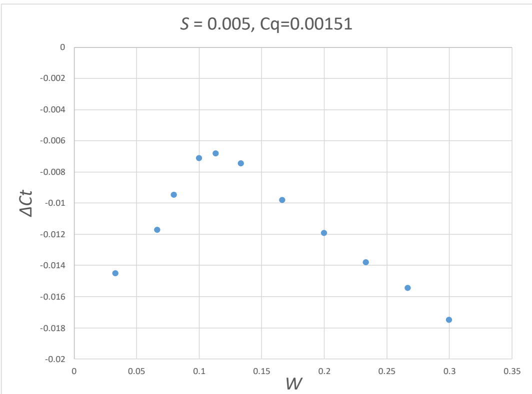


Fig. 6.9 axial thrust reduction by W

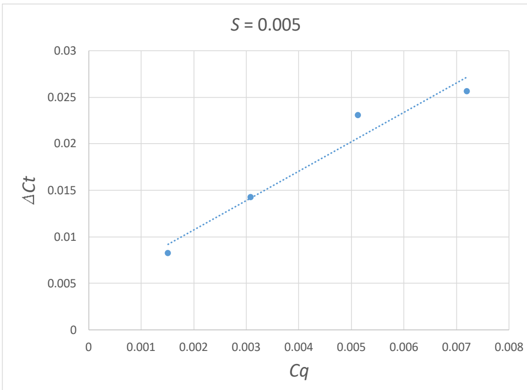


Fig. 6.10 axial thrust reduction by Cq

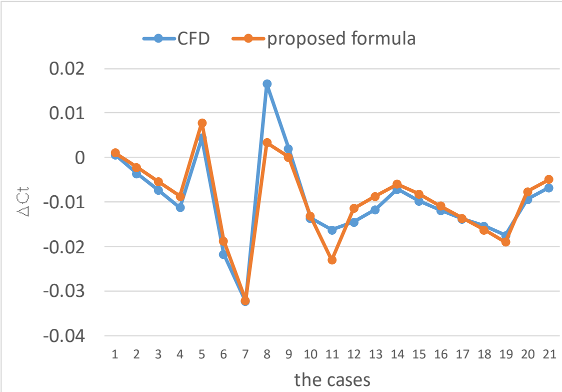


*Fig. 6.11 comparision between CFD and proposed formula (narrow gap, Cq ≠ 0)*

### 6.2.2 The estimation of effect of J-groove in intermediate gap

The radial pressure distributions in the intermediate gap are shown in section (4.2) for the case without through-flow and in section (5.3) for the case of inward through-flow. The CFD results are also compared. The dependence of the $\Delta C_t$ value on the parameters of J-groove from these pressure distributions will be calculated in this section.

#### 6.2.2.1 In intermediate gap without through-flow

The pressure distributions in no J-groove and with J-groove case in intermediate gap without throughflow are compared and shown in Fig. 4.8 to 4.12 with varies of J-groove parameters. Based on this discussion, the dependence of $\Delta C_t$ on the J-groove parameters is also investigated in this section and plotted in Fig. 6.12 to Fig. 6.15. It was very clear that, this dependence is linear with the number, depth, and width of J-groove. But in case of varies of width, although the reduction of axial thrust depends on the width of J-groove is linear, but it increased when $W < 0.2$ and decreased when $W > 0.2$ as shown in Fig. 6.14. So, the proposed formula for this case is given as:

$$\Delta Ct = a \times (n + b) \times (D + c) \times (L^2) \times (|W - 0.2| + d) \qquad (6.3)$$

with a = -0.9148; b = 10.83; c = -0.0043; d = 0.53; e = 0.1656

From this equation, the value of $\Delta C_t$ can be calculated with varying the J-groove parameter and give them into the Fig. 6.16 to make the comparison with the CFD results.

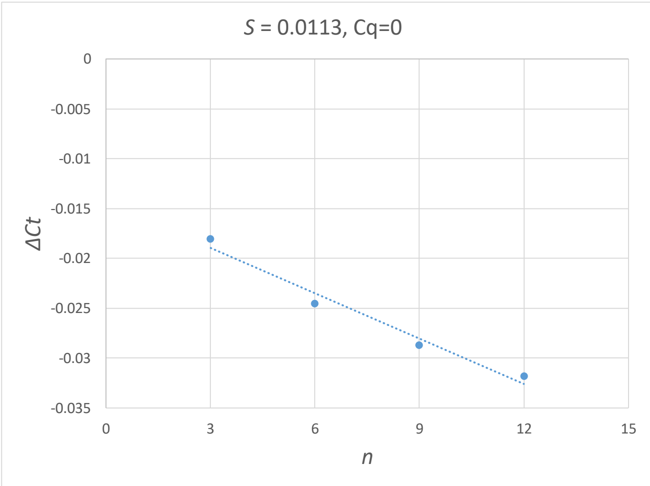


*Fig. 6.12 axial thrust reduction by n*

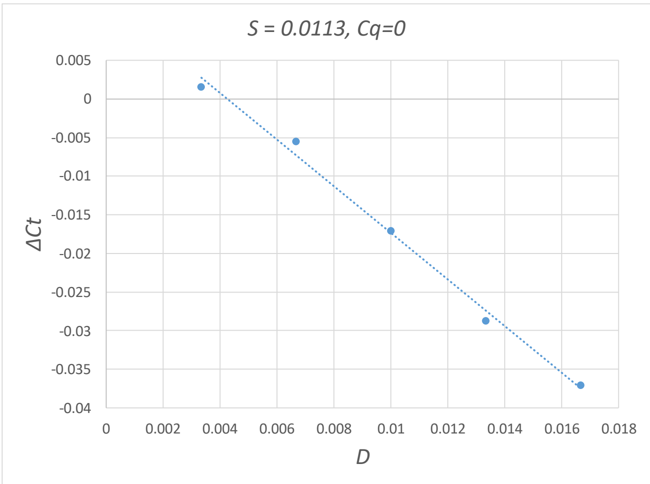


*Fig. 6.13 axial thrust reduction by D*

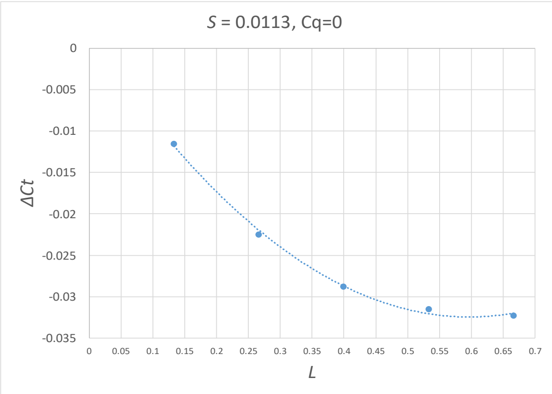


*Fig. 6.16 axial thrust reduction by L*

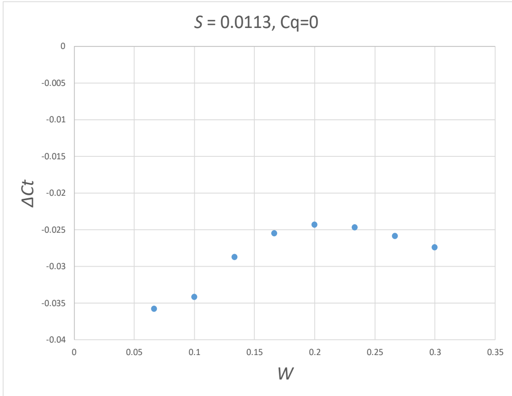


*Fig. 6.15 axial thrust reduction by W*

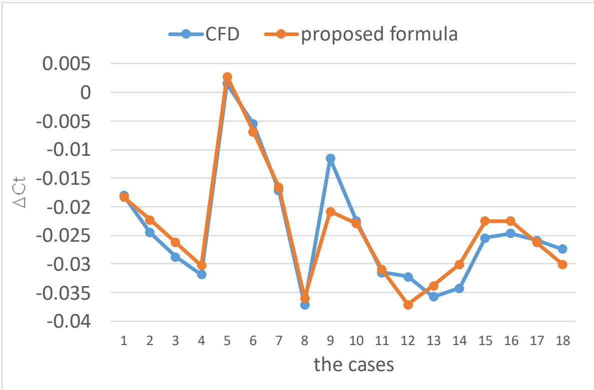


*Fig. 6.14 comparision between CFD and proposed formula (intermediate gap, Cq = 0)*

### 6.2.2.2 In intermediate gap with through-flow

Following on from the section (5.3), Fig. 6.17 to Fig. 6.20 shows the effect of axial thrust for varying J-groove parameters in the intermediate gap with through-flow. The radially inward throughflow takes angular momentum and considerable increases the tangential velocity, so that the pressure decreases, and the reduction of axial thrust increases as plotted in Fig. 6.21. This dependence is linear, and the dependence of $\Delta C_t$ on other parameters has the trending as in the case of without through-flow (In section 6.2.2.1). Therefore, the proposed formula can be written that:

$$\Delta Ct = a \times (n + b) \times (D + c) \times (L^2) \times (|W - 0.2| + d) \times Cq \qquad (6.4)$$

with a = -2.9386; b = 19.45; c = -0.007; d = 0.1388 from the different values of J-groove parameters given in Table 4-2 for the case of intermediate gap, the varies of $\Delta C_t$ were calculated based on the proposed formula (6.4) and plotted them into Fig. 6.22 to make the comparison with its values by CFD. There were some values get noticeable different, but the trend is almost the same.

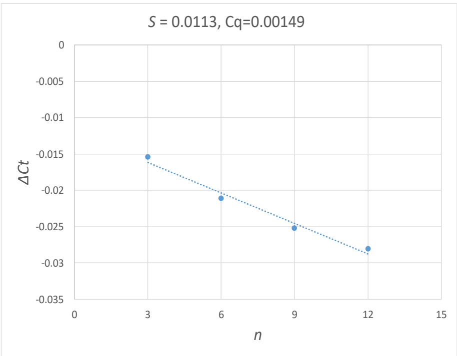


*Fig. 6.17 axial thrust reduction by n*

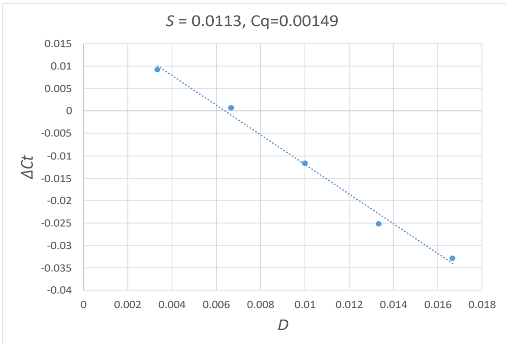


*Fig. 6.18 axial thrust reduction by D*

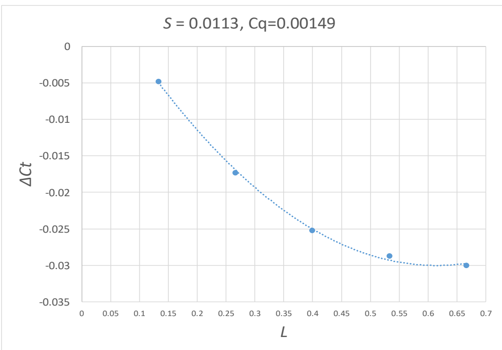


*Fig. 6.20 axial thrust reduction by L*

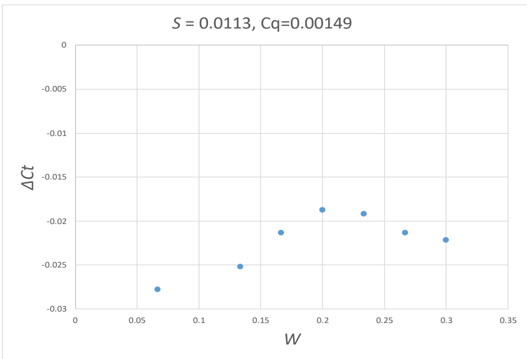


*Fig. 6.19 axial thrust reduction by W*

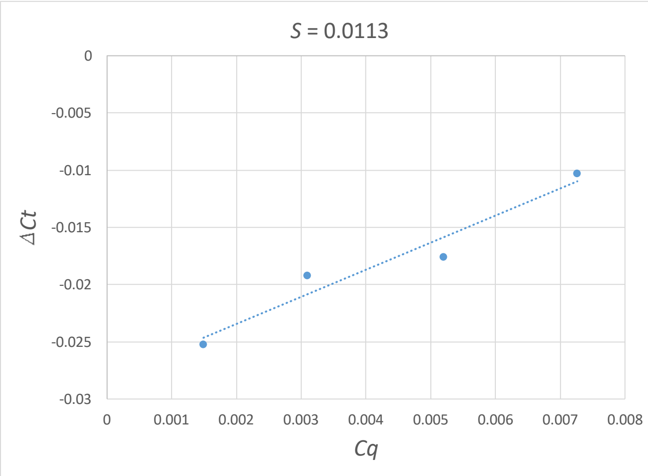


*Fig. 6.21 axial thrust reduction by Cq*

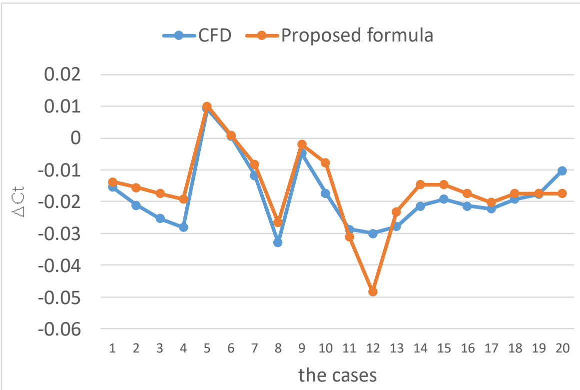


*Fig. 6.22 comparision between CFD and proposed formula (intermediate gap, $Cq \neq 0$)*

### 6.2.3 The estimation of effect of J-groove in large gap

The previous research reveals that the theory of non-interference gap gives good agreement with the case of a relatively large gap. The flow phenomenon and the pressure distributions in this gap were discussed in the section (4.3) and (5.4) for the case without and with throughflow, respectively.

#### 6.2.3.1 In large gap without through-flow

For the case of zero through-flow, the effect on various parameters of J-groove is shown in Fig. 6.23 to Fig. 6.26. Remaining the other J-groove geometry constant, when the number and the depth of groove is increased, the axial thrust coefficient $\Delta C_t$ is decreased significantly and linear. The effect of length of groove is presented in Fig. 6.25. It is also seen that, when the groove length increases, the reduction of thrust coefficient is also decreases as before. Unlike in the cases of narrow and intermediate gap, in the case of large gap, the thrust coefficient is almost constant when the width of J-groove is less than a certain value (here that value is equal 0.2), and then when the groove width is greater than that certain value, the axial thrust coefficient is reduced with increasing the groove width. The above-described dependence of axial thrust on J-groove parameters gives the axial thrust coefficient reduction $\Delta C_t$ defined in proposed formula such as:

$W < 0.2$ $$\Delta Ct = a \times (n) \times (D) \times (L^2 + b) \qquad (6.5)$$

with a = -0.1253 and b = 1.0802

$W > 0.2$ $$\Delta Ct = a \times (n) \times (D) \times (L^2 + b) \times (W + c) \qquad (6.6)$$

with a = -0.2372; b = 0.9138; c = 0.4444

from these formulas, the comparison of the results from the CFD and the results calculated by proposed formula was shown in Fig. 6.27.

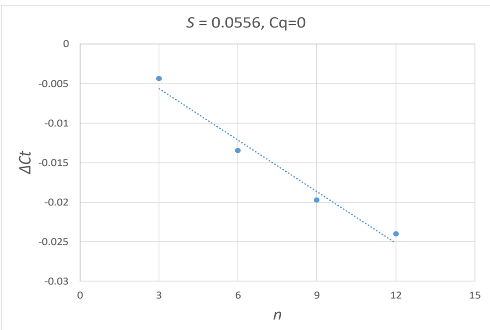


Fig. 6.24 axial thrust reduction by

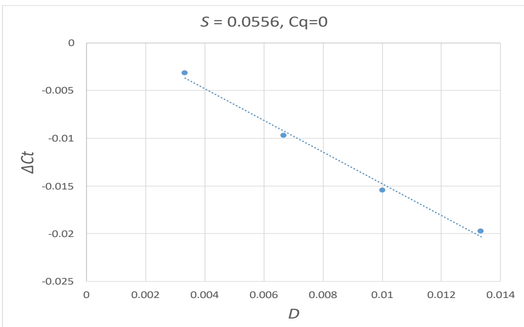


Fig. 6.23 axial thrust reduction by D

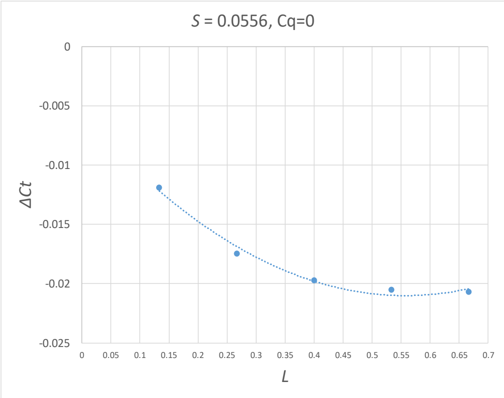


*Fig. 6.27 axial thrust reduction by L*

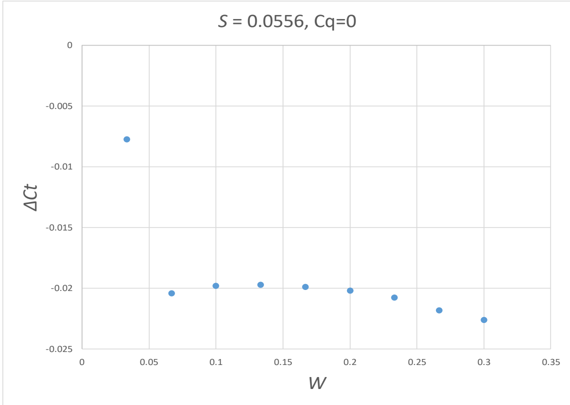


*Fig. 6.26 axial thrust reduction by W*

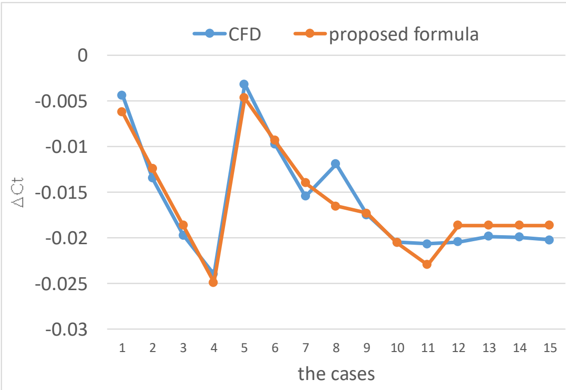


*Fig. 6.25 comparision between CFD and proposed formula (large gap, Cq = 0)*

### 6.2.3.2 In large gap with through-flow

The pressure distribution for the case of large gap with throughflow was investigated in section (5.4) before. From that, the axial thrust reduction by use of J-groove $\Delta C_t$ is calculated based on equation (3.1) and (3.2). Figure 6.28 to Fig. 6.31 show the effect of J-groove on axial thrust reduction and Fig. 6.32 presents the dependence of axial thrust on the flow rate coefficient *Cq*. Same as the case without throughflow in large gap (section 6.2.3.1), the dependence of axial thrust reduction $\Delta C_t$ on the number, the depth, and the flow rate coefficient *Cq* is linear as presented in Fig. 6.28; Fig. 6.29 and Fig 6.32, respectively. And likely with the case of zero through-flow, in the case of with throughflow in large gap, when the width of the groove is less than a certain value (here, 0.2), the axial thrust is almost constant; however, when the width of the groove is greater than that value, the axial thrust reduction decreases when increases the groove width. The proposed formula for this case is:

when $W < 0.2$,

$$\Delta Ct = a \times (n) \times (D + b) \times (L^2 + c) \times Cq \qquad (6.7)$$

a = -0.2696; b = -0.0048; c = 0.5152

when $W > 0.2$,

$$\Delta Ct = a \times (n) \times (D + b) \times (L^2 + c) \times (W + d) \times Cq \qquad (6.8)$$

a = -0.8785; b = -0.0047; c = 0.4072; d = 0.1966

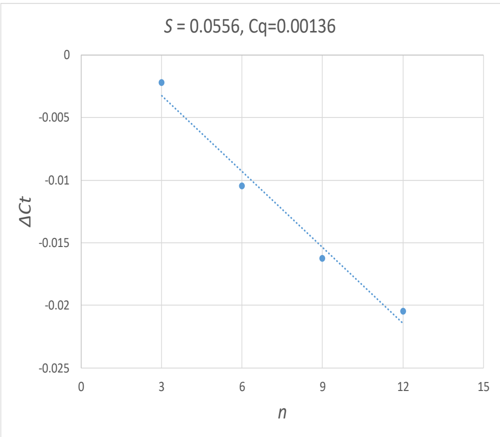


*Fig. 6.28 axial thrust reduction by n*

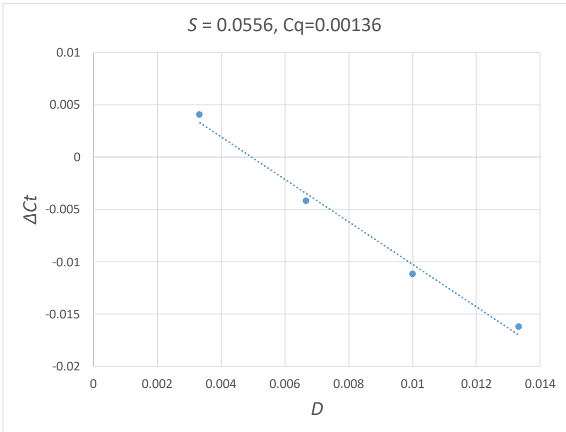


*Fig. 6.29 axial thrust reduction by D*

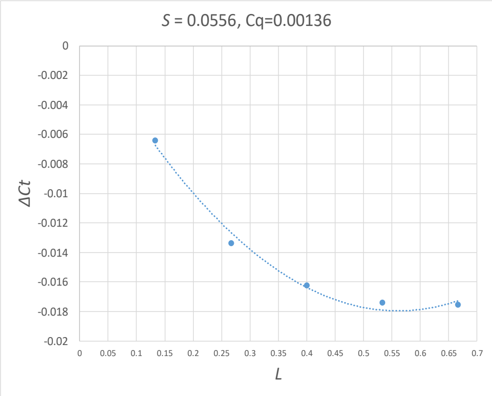


Fig. 6.30 axial thrust reduction by L

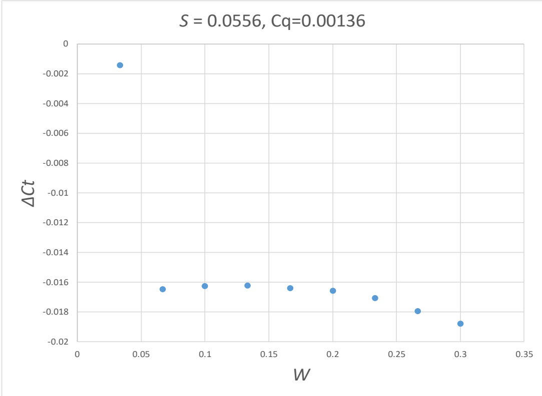


Fig. 6.31 axial thrust reduction by W

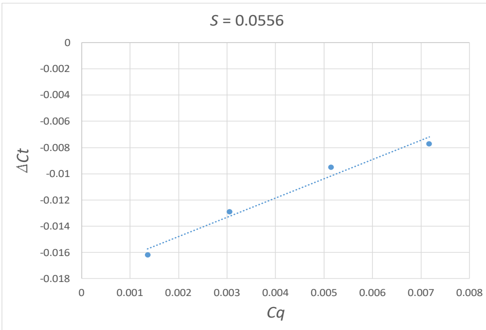


Fig. 6.32 axial thrust reduction by Cq

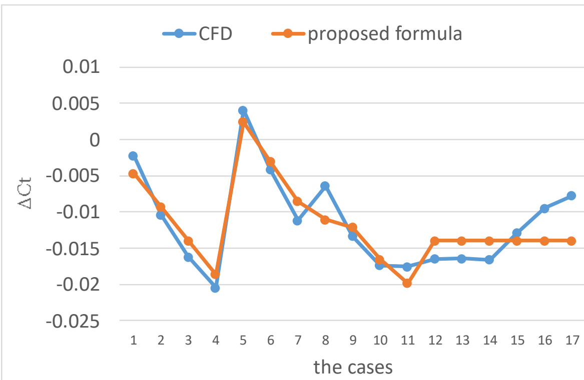


Fig. 6.33 comparision between CFD and proposed formula (large gap, $Cq \neq 0$)

### 6.3 Summary of Chapter 6

In this chapter, the influence of the J-groove parameters on the axial force reduction ratio has been presented to clearly see these effects. A prediction is then presented estimating the effect of the J-groove with different parameters on different gaps without or with through-flow. From the analysis of the results, the following conclusions can be drawn:

1 Cases of zero through-flow ($Cq$ = 0) in narrow, intermediate, and large gaps are investigated in sections (6.2.1.1); (6.2.2.1) and (6.2.3.1) but we can ignore them because the leakage flow always exist in the real cases.

2 Parameter groove width has some critical value for the effect of J-groove. In the intermediate gap and in the large gap cases, that critical value can be estimated as 0.2. Only in narrow gap case, that critical value is 0.12.

3 $\Delta C_t$ is proportional linear to J-groove number, depth, and flow rate coefficient $Cq$ for all cases.

4 According to the estimation of formula, we can design the J-Groove to get the adequate axial thrust force.

# Chapter 7

# Conclusion

# Chapter 7: Conclusion

## 7.1 Conclusion

The simulation of the flow in a rotor-stator cavity without and with J-groove based on the open-source code OpenFOAM has been presented. The parameter checking provides the optimal choice of discretization schemes, turbulence models, turbulence parameters, and necessary mesh refinement on the number of nodes of the rotor-stator cavity. This study confirms the calculated results using the provided k-omega SST turbulence model based on the experimental results in the absence of the J-groove and give an overview of the J-groove effect. A comparison was made with each other and with experimental data for no groove case. The parameters in the CFD model have been varied for the number, depth, length and width of the J-groove and the pressure distributions together with the velocity distributions have been investigated. The groove design parameters have been determined in relation to the impeller diameter. The results show that J-groove and proper location can increase the radial pressure curve completely. The velocity and pressure distribution have revealed the mechanism of the J-groove as follows: The groove flow mixes with the swirl flow of the rotating disk region and reduces the swirl strength and region of the reverse. The radial flow from the outer to inner causes a reduction of tangential velocity, as the result of transferred fluid with low angular momentum along the groove. Therefore, the present method uses the absorption of the angular momentum by mixing the groove flow with the swirl flow.

The present study found that the difference in pressure between the outer to the inner radius increases with increasing number, depth, and length of J-groove almost in all cases. Nevertheless, in the case of increasing the width of the J-groove pressure decreases when the ratio of the groove width to the outer radius $W$ is less than 0.12 in narrow gap and 0.2 in the intermediate gap and increases when $W$ is greater than 0.12 and 0.2 for narrow gap and intermediate gap, respectively. For the case of the large gap, the pressure distributions are almost the same when $W$ is less than 0.2 and increases when it is greater than 0.2. Also, when the coefficient depth of J-groove $D$ = 0.0033 for narrow gap and intermediate gap, or the length ratio $L$ =0.1333 for narrow gap without through-flow, the effect of J-groove is not improved due to increased hydraulic loss.

The influence of key geometrical parameters such as size and number of grooves, axial clearance, and flow rate have also been investigated. The results show that the superior effect of the J-groove in the radial grooves in the casing wall is due to two main reasons. First, the tangential velocity significantly reduces due to the mixing of the main flow and the groove flow. The second effect is an increase in radial velocity because of the reverse flow. Findings from this study indicate that J-groove is a common simple passive method to reduce axial thrust.

## 7.2 Outlook

Simple equations have been proposed in this study to easily predict the reduction in axial thrust, allowing estimation of new cases. The proposed method, however, has some limitations. First, to begin using the developed estimator, the type of gap (narrow, intermediate, or large) must be determined ahead of time. Second, the proposed formulas with varying Re numbers are not calculated. As a result, those formulas will need to be improved.

All results in this study are obtained using smooth disk. Surfaces rougher than those investigated in this study were not possible to obtain. It is also necessary to investigate how surface roughness affects the flow field for future work.

Because the suggested formulas are based on CFD results, their outcomes may differ from those of the experiments, that on real machines are required to validate the proposed formulas obtained in this thesis and demonstrate the applicability of the inferred correlations.

## 7.3 Future work

For future research, the effect of different *Re* or the flow with various through-flow should be considered. Moreover, further investigation is needed to suggest the optimal dimension and proper location of the grooves mounted on the casing wall to control and balance axial thrust in turbo machines. The positive effect of J-Groove on eddy flow suppression and turbocharging was examined by CFD analysis. Then, the optimized design of J-Groove will be implemented to improve the results.

## Related publications

The following are the most relevant publications to this thesis:

1）Vo Dao Nguyen, Jun Matsui: Numerical Analysis on the Effect of J-groove on Flows in Narrow Gaps between Rotating Disk and Casing, Journal of Fluid Machinery and Systems, Volume 15 Issue 1 Pages 64-74 (2022)

## Acknowledgements

I would like to express my deepest gratitude to Professor Matsui Jun, my supervisor, who has provided me with constant help, guidance, encouragement, and constructive criticism during the writing of this thesis. I'd also like to thank Professor Matsumoto Kazunari for regularly monitoring my lab meetings and sharing his valuable knowledge and experience.

I would like to express my sincerest thanks to Yokohama National University for having supported me financially during my 3 years studying there. In addition, the lecturers, and staff at YNU, especially Professor Takuto Araki, Professor Matsui Kazumi, and Professor Shimono Tomoyuki, are very kind and supportive.

I would like to thank former and current colleagues and friends in the computational fluid dynamics groups with whom I have had helpful discussions on occasion. I started this thesis without much knowledge of Linux, OpenFOAM and Computational Fluid Dynamics. Thank you to the students of Professor Matsui Jun's lab for more than three years of collaboration and for creating a vibrant and happy working atmosphere before the Covid pandemic hit.

I would like to express my gratitude to my former professors at Danang University, from whom I learned a lot about fluid mechanics and computational fluid dynamics.

I would also like to thank my wonderful friends in Japan and Vietnam who have been by my side to share my successes and disappointments over the years.

I dedicate this work to my wife, parents, and our family, as a tribute to their sacrifices, who have supported me throughout my life. Without them, this work would not have been completed.

## References


[1] J. Kurokawa and M. Sakuma, "Flow in a narrow gap along an enclosed rotating disk with through-flow," *Transactions of the Japan Society of Mechanical Engineers Series B*, vol. 53, no. 492, pp. 2468–2476, 1987, doi: 10.1299/kikaib.53.2468.

[2] T. Von Kármán, "On Laminar and Turbulent Friction," *Journal of Applied Mathematics and Mechanics*, vol. 1, pp. 233–252, 1921.

[3] J. W. Daily and R. E. Nece, "Chamber dimension effects on induced flow and frictional resistance of enclosed rotating disks," *Journal of Fluids Engineering, Transactions of the ASME*, vol. 82, no. 1, pp. 217–230, Mar. 1960, doi: 10.1115/1.3662532.

[4] E. M. Greitzer, J. P. Nikkanen, D. E. Haddad, R. S. Mazzawy, and H. D. Joslyn, "A fundamental criterion for the application of rotor casing treatment," *Journal of Fluids Engineering, Transactions of the ASME*, vol. 101, no. 2, pp. 237–243, Jun. 1979, doi: 10.1115/1.3448945.

[5] E. M. Greitzer, "The stability of pumping systems-the 1980 freeman scholar lecture," *Journal of Fluids Engineering, Transactions of the ASME*, vol. 103, no. 2, pp. 193–242, Jun. 1981, doi: 10.1115/1.3241725.

[6] J. K. and M. Sakuma and M. SAKURA, "Flow in a Narrow Gap Along an Enclosed Rotating disk with Through-Flow," *JSME international journal. Ser. 2, Fluids engineering, heat transfer, power, combustion, thermophysical properties*, vol. 31, no. 2, pp. 243–251, May 1988, doi: 10.1299/jsmeb1988.31.2_243.

[7] J. Kurokawa, K. Kamijo, and T. Shimura, "Axial thrust behavior in LOX-pump of rocket engine," *Journal of Propulsion and Power*, vol. 10, no. 2, pp. 244–250, 1994, doi: 10.2514/3.23735.

[8] J. Kurokawa, J. Matsui, S. L. Saha, and T. Kitahora, "Passive control of rotating stall in a parallel-wall vaneless diffuser by radial grooves," *Journal of Fluids Engineering, Transactions of the ASME*, vol. 122, no. 1, pp. 90–96, 2000, doi: 10.1115/1.483230.

[9] S. L. Saha, J. Kurokawa, J. Matsui, and H. Imamura, "Passive control of rotating stall in a parallel-wall vaned diffuser by J-Grooves," *Journal of Fluids Engineering, Transactions of the ASME*, vol. 123, no. 3, pp. 507–515, 2001, doi: 10.1115/1.1374214.

[10] J. KUROKAWA, M. INAGAKI, H. IMAMURA, T. TAGUCHI, K. NIIKURA, and J. MATSUI, "Transient Axial Thrust of High-Head Pump-Turbine at Load Rejection," *The proceedings of the JSME annual meeting*, vol. 2002.3, no. Vol.3, pp. 181–182, 2002, doi: 10.1299/jsmemecjo.2002.3.0_181.

[11] J. F. Gülich, "Disk friction losses of closed turbomachine impellers,"

*Forschung im Ingenieurwesen/Engineering Research*, vol. 68, no. 2, pp. 87–95, Dec. 2003, doi: 10.1007/S10010-003-0111-X.

[12] Y. Yamagishi and M. Oki, “Effect of the number of grooves on flow characteristics around a circular cylinder with triangular grooves,” *Journal of Visualization 2005 8:1*, vol. 8, no. 1, pp. 57–64, 2005, doi: 10.1007/BF03181603.

[13] S. Poncet, M. P. Chauve, and P. Le Gal, “Turbulent rotating disk flow with inward throughflow,” *Journal of Fluid Mechanics*, vol. 522, pp. 253–262, Jan. 2005, doi: 10.1017/S0022112004002046.

[14] H. Abe, K. Matsumoto, J. Kurokawa, J. Matsui, and Y.-D. Choi, “Analysis and Control of Axial Thrust in Centrifugal Pump by Use of J-Groove,” *Proc. of 23rd IAHR Symposium (CD-ROM)*, vol. 1, no. October, pp. 1–11, 2006, [Online]. Available: http://hdl.handle.net/10131/3700%0Ahttp://kamome.lib.ynu.ac.jp/dspace/handle/10131/3700.

[15] S. Poncet and R. Schiestel, “Numerical modeling of heat transfer and fluid flow in rotor-stator cavities with throughflow,” *International Journal of Heat and Mass Transfer*, vol. 50, no. 7–8, pp. 1528–1544, Apr. 2007, doi: 10.1016/j.ijheatmasstransfer.2006.08.028.

[16] Y. Do Choi, J. Kurokawa, and H. Imamura, “Suppression of cavitation in inducers by J-Grooves,” *Journal of Fluids Engineering, Transactions of the ASME*, vol. 129, no. 1, pp. 15–22, 2007, doi: 10.1115/1.2375126.

[17] J. Matsui, J. Kurokawa, H. Abe, and K. Matsumoto, “Study on control of axial thrust in centrifugal pump by use of J-Groove,” *Nihon Kikai Gakkai Ronbunshu, B Hen/Transactions of the Japan Society of Mechanical Engineers, Part B*, vol. 74, no. 2, pp. 317–322, 2008, doi: 10.1299/kikaib.74.317.

[18] “Vibration Induced by External Axial Flow,” *Flow Induced Vibrations*, pp. 107–144, Jan. 2008, doi: 10.1016/B978-0-08-044954-8.00003-6.

[19] R. Barrio, E. Blanco, J. Parrondo, J. González, and J. Fernández, “The Effect of Impeller Cutback on the Fluid-Dynamic Pulsations and Load at the Blade-Passing Frequency in a Centrifugal Pump,” *Journal of Fluids Engineering*, vol. 130, no. 11, pp. 1111021–11110211, Nov. 2008, doi: 10.1115/1.2969273.

[20] J. Kurokawa, H. Imamura, and Y.-D. Choi, “Effect of J-Groove on the Suppression of Swirl Flow in a Conical Diffuser,” *Journal of Fluids Engineering*, vol. 132, no. 7, Jul. 2010, doi: 10.1115/1.4001899.

[21] J. Matsui and T. Mugiyama, “Effect of J-Groove on the Axial Thrust in Centrifugal Pump,” *AIP Conference Proceedings*, vol. 1225, no. 1, p. 129, Jul. 2010, doi: 10.1063/1.3464851.

[22] M. T. Schobeiri, “Boundary Layer Theory,” *Fluid Mechanics for Engineers*, pp. 357–421, 2010, doi: 10.1007/978-3-642-11594-3_11.

[23] Y. Taamneh, “Numerical simulation of fluid flow in enclosed rotating filter and disk,” *Journal of Engineering and Applied Sciences*, vol. 5, no. 9, pp. 48–53, 2010.

[24] J. Kurokawa, “J-Groove Technique for Suppressing Various Anomalous Flow Phenomena in Turbomachines,” *Int. J. Fluid Mach. Syst.*, vol. 4, no. 1, pp. 1–13, 2011, doi: 10.5293/ijfms.2011.4.1.001.

[25] T. Shimura, S. Kawasaki, M. Uchiumi, T. Kimura, M. Hayashi, and J. Matsui, “Stability of an axial thrust self-balancing system,” *Journal of Fluids Engineering, Transactions of the ASME*, vol. 135, no. 1, pp. 1–11105, 2013, doi: 10.1115/1.4023197.

[26] P. Dupont, A. C. Bayeul-Lainé, A. Dazin, G. Bois, O. Roussette, and Q. Si, “Leakage flow simulation in a specific pump model,” *IOP Conference Series: Earth and Environmental Science*, vol. 22, 2014, doi: 10.1088/1755-1315/22/1/012012.

[27] A. Bhatia, “Theoretical analysis to calculate axial thrust in multistage centrifugal pumps,” *Institution of Mechanical Engineers - 12th European Fluid Machinery Congress*, pp. 159–171, Jan. 2014, doi: 10.1533/9780081001080.5.159.

[28] X. Q. Jia, B. L. Cui, Y. L. Zhang, and Z. C. Zhu, “Study on internal flow and external performance of a semi-open impeller centrifugal pump with different tip clearances,” *International Journal of Turbo and Jet Engines*, vol. 32, no. 1, pp. 1–12, Apr. 2015, doi: 10.1515/TJJ-2014-0010.

[29] S. Raza, S. H. Hejazi, and I. D. Gates, “Two phase flow of liquids in a narrow gap: Phase interference and hysteresis,” *Physics of Fluids*, vol. 28, no. 7, p. 074102, Jul. 2016, doi: 10.1063/1.4953238.

[30] M. P. Païdoussis, “Annular- and Leakage-Flow-Induced Instabilities,” *Fluid-Structure Interactions*, pp. 643–769, Jan. 2016, doi: 10.1016/B978-0-12-397333-7.00007-3.

[31] B. Hu, D. Brillert, H. J. Dohmen, and F. K. Benra, “Investigation on the flow in a rotor-stator cavity with centripetal through-flow,” *Int. J. Turbomachinery, Propuls. Power*, vol. 2, no. 4, 2017, doi: 10.3390/ijtpp2040018.

[32] T. V. Sanand, P. Pradeep Kumar, P. Unnikrishnan Nair, and P. P. George, “Numerical and experimental evaluation of performance of centrifugal seals,” *Sadhana - Academy Proceedings in Engineering Sciences*, vol. 42, no. 4, pp. 479–488, 2017, doi: 10.1007/s12046-017-0616-x.

[33] U. Shrestha and Y.-D. Choi, “A CFD-Based Shape Design Optimization Process of Fixed Flow Passages in a Francis Hydro Turbine,” *Processes*

*2020, Vol. 8, Page 1392*, vol. 8, no. 11, p. 1392, Oct. 2020, doi: 10.3390/PR8111392.

[34] T. Parikh, M. Mansour, and D. Thévenin, "Investigations on the effect of tip clearance gap and inducer on the transport of air-water two-phase flow by centrifugal pumps," *Chemical Engineering Science*, vol. 218, p. 115554, Jun. 2020, doi: 10.1016/J.CES.2020.115554.

# Appendix

## A.1. BlockMesh

```
FoamFile
{
    version     2.0;
    format      ascii;
    class       dictionary;
    object      blockMeshDict;
}
// * * * * * * * * * * * * * * * * * * * * * * * * * * * * * * * * * * * * * //
convertToMeters 1;
// ----  Setting  parameter ----
a  150e-3;            //radius of disk  (outer radius)
a1 30e-3;             //inner radius
ep 0.5e-3;            //thickness of inlet, outlet (disk radial-tip clearance)
ho 2e-3;              //height of outlet
hi 5e-3;              //height of inlet
s  0.005;            //radius ratio

n  9;                 //number Groove
d  1e-3;              //depth of Groove
l  60e-3;             //length of Groove
w  20e-3;             //width of Groove

PiAngle 180.0;
rotAngle #calc "2*$PiAngle /$n";
mrotAngle #calc "-$rotAngle";
Pirad       #calc "degToRad($PiAngle)";

epi         #calc "$ep";    //epi=ep;
epo         #calc "$ep";    //epo=ep;
h           #calc "$a*$s";  //h=a*s; height of Gap


aepi            #calc "$a+$epi";
aml             #calc "$a-$l";
a1epo           #calc "$a1+$epo";
```

```
alpha       #calc "$Pirad /$n";           //alpha=Pi/n; alpha rad
beta        #calc "asin($w /(2*$a))";     //beta=Asin(w/(2*a)); beta rad (to set width of Groove) on Circle outer radius a
beta1       #calc "asin($w /(2*$aepi))";  //beta1=Asin(w/(2*(a+epi))); beta rad on Circle1 radius a+epi
beta2       #calc "asin($w /(2*$aml))";   //beta2=Asin(w/(2*(a-l))); beta rad on Circle2 radius a-l
beta3       #calc "$beta2";               //beta3=beta2; beta rad on Circle3 radius a1+epo
beta4       #calc "$beta2";               //beta4=beta2; beta rad on Circle4 inner radius a1

betaf       #calc "($alpha+$beta) /2";
beta1f      #calc "($alpha+$beta1) /2";
beta2f      #calc "($alpha+$beta2) /2";
beta3f      #calc "($alpha+$beta3) /2";
beta4f      #calc "($alpha+$beta4) /2";

h2          #calc "$hi+$h";                 //h2=hi+h; height of inlet+gap
h3          #calc "$h2+$ho";                //h3=h2+ho;
hj          #calc "$h2+$d";                 //hj=h2+d;

sinalpha    #calc "sin($alpha)";            //sinalpha=Sin(alpha);
cosalpha    #calc "cos($alpha)";            //cosalpha=Cos(alpha);

sinbeta     #calc "sin($beta)";             //sinbeta=Sin(beta);
cosbeta     #calc "cos($beta)";             //cosbeta=Cos(beta);

sinbeta1    #calc "sin($beta1)";            //sinbeta1=Sin(beta1);
cosbeta1    #calc "cos($beta1)";            //cosbeta1=Cos(beta1);

sinbeta2    #calc "sin($beta2)";            //sinbeta2=Sin(beta2);
cosbeta2    #calc "cos($beta2)";            //cosbeta2=Cos(beta2);

sinbeta3    #calc "sin($beta3)";            //sinbeta3=Sin(beta3);
cosbeta3    #calc "cos($beta3)";            //cosbeta3=Cos(beta3);

sinbeta4    #calc "sin($beta4)";            //sinbeta4=Sin(beta4);
cosbeta4    #calc "cos($beta4)";            //cosbeta4=Cos(beta4);

acosalpha   #calc "$a*$cosalpha";
asinalpha   #calc "$a*$sinalpha";
masinalpha  #calc "-$asinalpha";

aepicosalpha     #calc "$aepi*$cosalpha";
aepisinalpha     #calc "$aepi*$sinalpha";
maepisinalpha    #calc "-$aepisinalpha";

amlcosalpha      #calc "$aml*$cosalpha";
amlsinalpha      #calc "$aml*$sinalpha";
mamlsinalpha     #calc "-$amlsinalpha";

a1epocosalpha    #calc "$a1epo*$cosalpha";
a1eposinalpha    #calc "$a1epo*$sinalpha";
ma1eposinalpha   #calc "-$a1eposinalpha";
a1cosalpha       #calc "$a1*$cosalpha";
a1sinalpha       #calc "$a1*$sinalpha";
ma1sinalpha      #calc "-$a1sinalpha";

acosbeta         #calc "$a*$cosbeta";
asinbeta         #calc "$a*$sinbeta";
masinbeta        #calc "-$asinbeta";

aepicosbeta1     #calc "$aepi*$cosbeta1";
aepisinbeta1     #calc "$aepi*$sinbeta1";
maepisinbeta1    #calc "-$aepisinbeta1";

amlcosbeta2      #calc "$aml*$cosbeta2";
amlsinbeta2      #calc "$aml*$sinbeta2";
mamlsinbeta2     #calc "-$amlsinbeta2";

a1epocosbeta3    #calc "$a1epo*$cosbeta3";
a1eposinbeta3    #calc "$a1epo*$sinbeta3";
ma1eposinbeta3   #calc "-$a1eposinbeta3";

a1cosbeta4       #calc "$a1*$cosbeta4";
a1sinbeta4       #calc "$a1*$sinbeta4";
ma1sinbeta4      #calc "-$a1sinbeta4";
```

```
sinbetaf     #calc "sin($betaf)";              //sinbeta=Sin(beta);
cosbetaf     #calc "cos($betaf)";              //cosbeta=Cos(beta);
sinbeta1f    #calc "sin($beta1f)";             //sinbeta1=Sin(beta1);
cosbeta1f    #calc "cos($beta1f)";             //cosbeta1=Cos(beta1);
sinbeta2f    #calc "sin($beta2f)";             //sinbeta2=Sin(beta2);
cosbeta2f    #calc "cos($beta2f)";             //cosbeta2=Cos(beta2);
sinbeta3f    #calc "sin($beta3f)";             //sinbeta3=Sin(beta3);
cosbeta3f    #calc "cos($beta3f)";             //cosbeta3=Cos(beta3);
sinbeta4f    #calc "sin($beta4f)";             //sinbeta4=Sin(beta4);
cosbeta4f    #calc "cos($beta4f)";

acosbetaf        #calc "$a*$cosbetaf";
asinbetaf        #calc "$a*$sinbetaf";
masinbetaf       #calc "-$asinbetaf";

aepicosbeta1f    #calc "$aepi*$cosbeta1f";
aepisinbeta1f    #calc "$aepi*$sinbeta1f";
maepisinbeta1f   #calc "-$aepisinbeta1f";

amlcosbeta2f     #calc "$aml*$cosbeta2f";
amlsinbeta2f     #calc "$aml*$sinbeta2f";
mamlsinbeta2f    #calc "-$amlsinbeta2f";

a1epocosbeta3f   #calc "$a1epo*$cosbeta3f";
a1eposinbeta3f   #calc "$a1epo*$sinbeta3f";
ma1eposinbeta3f  #calc "-$a1eposinbeta3f";

a1cosbeta4f      #calc "$a1*$cosbeta4f";
a1sinbeta4f      #calc "$a1*$sinbeta4f";
ma1sinbeta4f     #calc "-$a1sinbeta4f";
//
N1i   12;
pcl1i1    0.5;
pccell1i1 0.5;
Rx1i1 5;
inRx1i1 0.2;
pcl1i2          #calc "1.0-$pcl1i1";
pccell1i2       #calc "1.0-$pccell1i1";
Rx1i2           #calc "$inRx1i1";

N1o   8;
pcl1o1    0.5;
pccell1o1 0.5;
Rx1o1 4;
inRx1o1 0.25;
pcl1o2          #calc "1.0-$pcl1o1";
pccell1o2       #calc "1.0-$pccell1o1";
Rx1o2           #calc "$inRx1o1";

N2    46;
pcl21     0.4;
pccell21 0.5;
Rx21 8;
inRx21 0.125;
pcl22           #calc "1.0-$pcl21";
pccell22        #calc "1.0-$pccell21";
Rx22 0.5;
inRx22 2;

N3    40;
pcl31     0.5;
pccell31 0.5;
Rx31 5;
inRx31 0.2;
pcl32           #calc "1.0-$pcl31";
pccell32        #calc "1.0-$pccell31";
Rx32            #calc "$inRx31";

N4    40;
pcl41     0.1;
pccell41 0.2;
Rx41 10;
pcl42     0.3;
pccell42 0.25;
Rx42 1;
pcl43           #calc "1.0-$pcl41-$pcl42";
pccell43        #calc "1.0-$pccell41-$pccell42";
Rx43 0.4;

N5    58;
pcl51     0.2;
pccell51 0.2;
Rx51 1.5;
pcl52     0.75;
pccell52 0.6;
Rx52 1;
pcl53           #calc "1.0-$pcl51-$pcl52";
pccell53        #calc "1.0-$pccell51-$pccell52";
Rx53 0.05;

N6o   12;
Rx6o1 10;
pcl6o1    0.8;
pccell6o1 0.6;
Rx6o2 0.6;
pcl6o2   #calc "1.0-$pcl6o1";
pccell6o2 #calc "1.0-$pccell6o1";

N6i   30;
pcl6i1    0.8;
pccell6i1 0.6;
Rx6i1 1.5;
inRx6i1 0.667;
pcl6i2          #calc "1.0-$pcl6i1";
pccell6i2       #calc "1.0-$pccell6i1";
Rx6i2 0.1;

Ng    22;
pclg1     0.5;
pccellg1 0.5;
Rxg1 5;
inRxg1 0.2;
pclg2           #calc "1.0-$pclg1";
pccellg2        #calc "1.0-$pccellg1";
Rxg2            #calc "$inRxg1";

Nj    26;
pclj1     0.5;
pccellj1 0.5;
Rxj1 5;
inRxj1 0.2;
pclj2           #calc "1.0-$pclj1";
pccellj2        #calc "1.0-$pccellj1";
Rxj2            #calc "$inRxj1";
// -----------------------------
```

```
vertices
(
//Create points at z = h2
    ($acosalpha $asinalpha $h2)          //0  left on Circle outer radius a
    ($acosalpha $masinalpha $h2)         //  right on Circle outer radius a
    ($aepicosalpha $aepisinalpha $h2)    //2  left on Circle outer radius a+epi
    ($aepicosalpha $maepisinalpha $h2)   // right on Circle outer radius a+epi
    ($amlcosalpha $amlsinalpha $h2)      //4  left on Circle outer radius a-l
    ($amlcosalpha $mamlsinalpha $h2)     // right on Circle outer radius a-l

    ($a1epocosalpha $a1eposinalpha $h2)  //6  left on Circle outer radius a1+epo
    ($a1epocosalpha $ma1eposinalpha $h2) //  right on Circle outer radius a1+epo
    ($a1cosalpha $a1sinalpha $h2)        //8  left on Circle outer radius a1
    ($a1cosalpha $ma1sinalpha $h2)       //  right on Circle outer radius a1

    ($acosbeta $asinbeta $h2)            //10
    ($acosbeta $masinbeta $h2)           //
    ($aepicosbeta1 $aepisinbeta1 $h2)    //12
    ($aepicosbeta1 $maepisinbeta1 $h2)   //
    ($amlcosbeta2 $amlsinbeta2 $h2)      //14
    ($amlcosbeta2 $mamlsinbeta2 $h2)     //
    ($a1epocosbeta3 $a1eposinbeta3 $h2)  //16
    ($a1epocosbeta3 $ma1eposinbeta3 $h2) //
    ($a1cosbeta4 $a1sinbeta4 $h2)        //18
    ($a1cosbeta4 $ma1sinbeta4 $h2)       //

    ($acosalpha $asinalpha $hi)          //20  left on Circle outer radius a
    ($acosalpha $masinalpha $hi)         //  right on Circle outer radius a
    ($aepicosalpha $aepisinalpha $hi)    //22  left on Circle outer radius a+epi
    ($aepicosalpha $maepisinalpha $hi)   //  right on Circle outer radius a+epi
    ($amlcosalpha $amlsinalpha $hi)      //24  left on Circle outer radius a-l
    ($amlcosalpha $mamlsinalpha $hi)     //  right on Circle outer radius a-l
    ($a1epocosalpha $a1eposinalpha $hi)  //26  left on Circle outer radius a1+epo
    ($a1epocosalpha $ma1eposinalpha $hi) //  right on Circle outer radius a1+epo
    ($a1cosalpha $a1sinalpha $hi)        //28  left on Circle outer radius a1
    ($a1cosalpha $ma1sinalpha $hi)       //  right on Circle outer radius a1

    ($acosbeta $asinbeta $hi)            //30
    ($acosbeta $masinbeta $hi)           //
    ($aepicosbeta1 $aepisinbeta1 $hi)    //32
    ($aepicosbeta1 $maepisinbeta1 $hi)   //
    ($amlcosbeta2 $amlsinbeta2 $hi)      //34
    ($amlcosbeta2 $mamlsinbeta2 $hi)     //
    ($a1epocosbeta3 $a1eposinbeta3 $hi)  //36
    ($a1epocosbeta3 $ma1eposinbeta3 $hi) //
    ($a1cosbeta4 $a1sinbeta4 $hi)        //38
    ($a1cosbeta4 $ma1sinbeta4 $hi)       //39

    ($a1epocosalpha $a1eposinalpha $h3)  //40  left on Circle outer radius a1+epo
    ($a1epocosalpha $ma1eposinalpha $h3) //  right on Circle outer radius a1+epo
    ($a1cosalpha $a1sinalpha $h3)        //42  left on Circle outer radius a1
    ($a1cosalpha $ma1sinalpha $h3)       //  right on Circle outer radius a1
    ($a1epocosbeta3 $a1eposinbeta3 $h3)  //44
    ($a1epocosbeta3 $ma1eposinbeta3 $h3) //
    ($a1cosbeta4 $a1sinbeta4 $h3)        //46
    ($a1cosbeta4 $ma1sinbeta4 $h3)       //

    ($acosalpha $asinalpha 0)            //48  left on Circle outer radius a
    ($acosalpha $masinalpha 0)           //  right on Circle outer radius a
    ($aepicosalpha $aepisinalpha 0)      //50  left on Circle outer radius a+epi
    ($aepicosalpha $maepisinalpha 0)     // right on Circle outer radius a+epi
    ($acosbeta $asinbeta 0)              //52
    ($acosbeta $masinbeta 0)             //
    ($aepicosbeta1 $aepisinbeta1 0)      //54
    ($aepicosbeta1 $maepisinbeta1 0)     //

    ($acosbeta $asinbeta $hj)            //56
    ($acosbeta $masinbeta $hj)           //
    ($aepicosbeta1 $aepisinbeta1 $hj)    //58
    ($aepicosbeta1 $maepisinbeta1 $hj)   //
    ($amlcosbeta2 $amlsinbeta2 $hj)      //60
    ($amlcosbeta2 $mamlsinbeta2 $hj)     //
);
```

```
blocks
(
//block inlet
    hex (49 51 55 53 21 23 33 31) ($N1i $N2 $N6i)     //block0 R
    simpleGrading
    (
        (($pcl1i1 $pccell1i1 $Rx1i1) ($pcl1i2 $pccell1i2 $Rx1i2))
        (($pcl22 $pccell22 $inRx22) ($pcl21 $pccell21 $inRx21))
        (($pcl6i1 $pccell6i1 $Rx6i1) ($pcl6i2 $pccell6i2 $Rx6i2))
    )

    hex (53 55 54 52 31 33 32 30) ($N1i $N3 $N6i)     //block1
    simpleGrading
    (
        (($pcl1i1 $pccell1i1 $Rx1i1) ($pcl1i2 $pccell1i2 $Rx1i2))
        (($pcl31 $pccell31 $Rx31) ($pcl32 $pccell32 $Rx32))
        (($pcl6i1 $pccell6i1 $Rx6i1) ($pcl6i2 $pccell6i2 $Rx6i2))
    )

    hex (52 54 50 48 30 32 22 20) ($N1i $N2 $N6i)     //block2 L
    simpleGrading
    (
        (($pcl1i1 $pccell1i1 $Rx1i1) ($pcl1i2 $pccell1i2 $Rx1i2))
        (($pcl21 $pccell21 $Rx21) ($pcl22 $pccell22 $Rx22))
        (($pcl6i1 $pccell6i1 $Rx6i1) ($pcl6i2 $pccell6i2 $Rx6i2))
    )

//block gap
    hex (21 23 33 31 1 3 13 11) ($N1i $N2 $Ng)        //block3 R
    simpleGrading
    (
        (($pcl1i1 $pccell1i1 $Rx1i1) ($pcl1i2 $pccell1i2 $Rx1i2))
        (($pcl22 $pccell22 $inRx22) ($pcl21 $pccell21 $inRx21))
        (($pclg1 $pccellg1 $Rxg1) ($pclg2 $pccellg2 $Rxg2))
    )

    hex (31 33 32 30 11 13 12 10) ($N1i $N3 $Ng)      //block4
    simpleGrading
    (
        (($pcl1i1 $pccell1i1 $Rx1i1) ($pcl1i2 $pccell1i2 $Rx1i2))
        (($pcl31 $pccell31 $Rx31) ($pcl32 $pccell32 $Rx32))
        (($pclg1 $pccellg1 $Rxg1) ($pclg2 $pccellg2 $Rxg2))
    )

    hex (30 32 22 20 10 12 2 0) ($N1i $N2 $Ng)        //block5 L
    simpleGrading
    (
        (($pcl1i1 $pccell1i1 $Rx1i1) ($pcl1i2 $pccell1i2 $Rx1i2))
        (($pcl21 $pccell21 $Rx21) ($pcl22 $pccell22 $Rx22))
        (($pclg1 $pccellg1 $Rxg1) ($pclg2 $pccellg2 $Rxg2))
    )


    hex (25 21 31 35 5 1 11 15) ($N5 $N2 $Ng)         //block6 R
    simpleGrading
    (
        (($pcl51 $pccell51 $Rx51) ($pcl52 $pccell52 $Rx52) ($pcl53 $pccell53 $Rx53))
        (($pcl22 $pccell22 $inRx22) ($pcl21 $pccell21 $inRx21))
        (($pclg1 $pccellg1 $Rxg1) ($pclg2 $pccellg2 $Rxg2))
    )

    hex (35 31 30 34 15 11 10 14) ($N5 $N3 $Ng)       //block7
    simpleGrading
    (
        (($pcl51 $pccell51 $Rx51) ($pcl52 $pccell52 $Rx52) ($pcl53 $pccell53 $Rx53))
        (($pcl31 $pccell31 $Rx31) ($pcl32 $pccell32 $Rx32))
        (($pclg1 $pccellg1 $Rxg1) ($pclg2 $pccellg2 $Rxg2))
    )

    hex (34 30 20 24 14 10 0 4) ($N5 $N2 $Ng)         //block8 L
    simpleGrading
    (
        (($pcl51 $pccell51 $Rx51) ($pcl52 $pccell52 $Rx52) ($pcl53 $pccell53 $Rx53))
        (($pcl21 $pccell21 $Rx21) ($pcl22 $pccell22 $Rx22))
        (($pclg1 $pccellg1 $Rxg1) ($pclg2 $pccellg2 $Rxg2))
    )
```

```
    hex (27 25 35 37 7 5 15 17) ($N4 $N2 $Ng)          //block9 R
    simpleGrading
    (
        (($pcl41 $pccell41 $Rx41) ($pcl42 $pccell42 $Rx42) ($pcl43 $pccell43 $Rx43))
        (($pcl22 $pccell22 $inRx22) ($pcl21 $pccell21 $inRx21))
        (($pclg1 $pccellg1 $Rxg1) ($pclg2 $pccellg2 $Rxg2))
    )

    hex (37 35 34 36 17 15 14 16) ($N4 $N3 $Ng)        //block10
    simpleGrading
    (
        (($pcl41 $pccell41 $Rx41) ($pcl42 $pccell42 $Rx42) ($pcl43 $pccell43 $Rx43))
        (($pcl31 $pccell31 $Rx31) ($pcl32 $pccell32 $Rx32))
        (($pclg1 $pccellg1 $Rxg1) ($pclg2 $pccellg2 $Rxg2))
    )

    hex (36 34 24 26 16 14 4 6) ($N4 $N2 $Ng)          //block11 L
    simpleGrading
    (
        (($pcl41 $pccell41 $Rx41) ($pcl42 $pccell42 $Rx42) ($pcl43 $pccell43 $Rx43))
        (($pcl21 $pccell21 $Rx21) ($pcl22 $pccell22 $Rx22))
        (($pclg1 $pccellg1 $Rxg1) ($pclg2 $pccellg2 $Rxg2))
    )

    hex (29 27 37 39 9 7 17 19) ($N1o $N2 $Ng)         //block12 R
    simpleGrading
    (
        (($pcl1o1 $pccell1o1 $Rx1o1) ($pcl1o2 $pccell1o2 $Rx1o2))
        (($pcl22 $pccell22 $inRx22) ($pcl21 $pccell21 $inRx21))
        (($pclg1 $pccellg1 $Rxg1) ($pclg2 $pccellg2 $Rxg2))
    )

    hex (39 37 36 38 19 17 16 18) ($N1o $N3 $Ng)       //block13
    simpleGrading
    (
        (($pcl1o1 $pccell1o1 $Rx1o1) ($pcl1o2 $pccell1o2 $Rx1o2))
        (($pcl31 $pccell31 $Rx31) ($pcl32 $pccell32 $Rx32))
        (($pclg1 $pccellg1 $Rxg1) ($pclg2 $pccellg2 $Rxg2))
    )

    hex (38 36 26 28 18 16 6 8) ($N1o $N2 $Ng)         //block14 L
    simpleGrading
    (
        (($pcl1o1 $pccell1o1 $Rx1o1) ($pcl1o2 $pccell1o2 $Rx1o2))
        (($pcl21 $pccell21 $Rx21) ($pcl22 $pccell22 $Rx22))
        (($pclg1 $pccellg1 $Rxg1) ($pclg2 $pccellg2 $Rxg2))
    )

//block outlet
    hex (9 7 17 19 43 41 45 47) ($N1o $N2 $N6o)        //block15 R
    simpleGrading
    (
        (($pcl1o1 $pccell1o1 $Rx1o1) ($pcl1o2 $pccell1o2 $Rx1o2))
        (($pcl22 $pccell22 $inRx22) ($pcl21 $pccell21 $inRx21))
        (($pcl6o2 $pccell6o2 $Rx6o1) ($pcl6o1 $pccell6o1 $Rx6o2))
    )

    hex (19 17 16 18 47 45 44 46) ($N1o $N3 $N6o)       //block16
    simpleGrading
    (
        (($pcl1o1 $pccell1o1 $Rx1o1) ($pcl1o2 $pccell1o2 $Rx1o2))
        (($pcl31 $pccell31 $Rx31) ($pcl32 $pccell32 $Rx32))
        (($pcl6o2 $pccell6o2 $Rx6o1) ($pcl6o1 $pccell6o1 $Rx6o2))
    )

    hex (18 16 6 8 46 44 40 42) ($N1o $N2 $N6o)         //block17 L
    simpleGrading
    (
        (($pcl1o1 $pccell1o1 $Rx1o1) ($pcl1o2 $pccell1o2 $Rx1o2))
        (($pcl21 $pccell21 $Rx21) ($pcl22 $pccell22 $Rx22))
        (($pcl6o2 $pccell6o2 $Rx6o1) ($pcl6o1 $pccell6o1 $Rx6o2))
    )

//block groove
    hex (11 13 12 10 57 59 58 56) ($N1i $N3 $Nj)        //block18
    simpleGrading
    (
        (($pcl1i1 $pccell1i1 $Rx1i1) ($pcl1i2 $pccell1i2 $Rx1i2))
        (($pcl31 $pccell31 $Rx31) ($pcl32 $pccell32 $Rx32))
        (($pclj1 $pccellj1 $Rxj1) ($pclj2 $pccellj2 $Rxj2))
    )

    hex (15 11 10 14 61 57 56 60) ($N5 $N3 $Nj)         //block19
    simpleGrading
    (
        (($pcl51 $pccell51 $Rx51) ($pcl52 $pccell52 $Rx52) ($pcl53 $pccell53 $Rx53))
        (($pcl31 $pccell31 $Rx31) ($pcl32 $pccell32 $Rx32))
        (($pclj1 $pccellj1 $Rxj1) ($pclj2 $pccellj2 $Rxj2))
    )

);
```

```
edges
(
    arc 49 53($acosbetaf $masinbetaf 0)
    arc 53 52($a 0 0)
    arc 52 48($acosbetaf $asinbetaf 0)
    arc 51 55($aepicosbeta1f $maepisinbeta1f 0)
    arc 55 54($aepi 0 0)
    arc 54 50($aepicosbeta1f $aepisinbeta1f 0)


    arc 29 39($a1cosbeta4f $ma1sinbeta4f $hi)
    arc 39 38($a1 0 $hi)
    arc 38 28($a1cosbeta4f $a1sinbeta4f $hi)

    arc 27 37($a1epocosbeta3f $ma1eposinbeta3f $hi)
    arc 37 36($a1epo 0 $hi)
    arc 36 26($a1epocosbeta3f $a1eposinbeta3f $hi)

    arc 25 35($amlcosbeta2f $mamlsinbeta2f $hi)
    arc 35 34($aml 0 $hi)
    arc 34 24($amlcosbeta2f $amlsinbeta2f $hi)

    arc 21 31($acosbetaf $masinbetaf $hi)
    arc 31 30($a 0 $hi)
    arc 30 20($acosbetaf $asinbetaf $hi)

    arc 23 33($aepicosbeta1f $maepisinbeta1f $hi)
    arc 33 32($aepi 0 $hi)
    arc 32 22($aepicosbeta1f $aepisinbeta1f $hi)


    arc 9 19($a1cosbeta4f $ma1sinbeta4f $h2)
    arc 19 18($a1 0 $h2)
    arc 18 8($a1cosbeta4f $a1sinbeta4f $h2)

    arc 7 17($a1epocosbeta3f $ma1eposinbeta3f $h2)
    arc 17 16($a1epo 0 $h2)
    arc 16 6($a1epocosbeta3f $a1eposinbeta3f $h2)

    arc 5 15($amlcosbeta2f $mamlsinbeta2f $h2)
    arc 15 14($aml 0 $h2)
    arc 14 4($amlcosbeta2f $amlsinbeta2f $h2)

    arc 1 11($acosbetaf $masinbetaf $h2)
    arc 11 10($a 0 $h2)
    arc 10 0($acosbetaf $asinbetaf $h2)

    arc 3 13($aepicosbeta1f $maepisinbeta1f $h2)
    arc 13 12($aepi 0 $h2)
    arc 12 2($aepicosbeta1f $aepisinbeta1f $h2)


    arc 43 47($a1cosbeta4f $ma1sinbeta4f $h3)
    arc 47 46($a1 0 $h3)
    arc 46 42($a1cosbeta4f $a1sinbeta4f $h3)

    arc 41 45($a1epocosbeta3f $ma1eposinbeta3f $h3)
    arc 45 44($a1epo 0 $h3)
    arc 44 40($a1epocosbeta3f $a1eposinbeta3f $h3)


    arc 61 60($aml 0 $hj)
    arc 57 56($a 0 $hj)
    arc 59 58($aepi 0 $hj)
);
boundary
(
    wallStator
    {
        type wall;
        faces
        (
            (51 55 33 23)
            (55 54 32 33)
            (54 50 22 32)
            (23 33 13 3)
            (33 32 12 13)
            (32 22 2 12)
            (13 12 58 59)
            (15 61 60 14)
            (7 17 45 41)
            (17 16 44 45)
            (16 6 40 44)
            (15 11 57 61)
            (11 13 59 57)
            (14 60 56 10)
            (10 56 58 12)
            (3 13 11 1)
            (1 11 15 5)
            (5 15 17 7)
            (59 58 56 57)
            (57 56 60 61)
            (15 14 16 17)
            (12 2 0 10)
            (10 0 4 14)
            (14 4 6 16)
        );
    }
```

```
    wallRotor
    {
        type wall;
        faces
        (
            (49 21 31 53)
            (53 31 30 52)
            (52 30 20 48)
            (29 9 19 39)
            (39 19 18 38)
            (38 18 8 28)
            (9 43 47 19)
            (19 47 46 18)
            (18 46 42 8)
            (27 29 39 37)
            (37 39 38 36)
            (36 38 28 26)
            (25 27 37 35)
            (35 37 36 34)
            (34 36 26 24)
            (21 25 35 31)
            (31 35 34 30)
            (30 34 24 20)
        );
    }
    outlet
    {
        type patch;
        faces
        (
            (41 45 47 43)
            (45 44 46 47)
            (44 40 42 46)
        );
    }
    inlet
    {
        type patch;
        faces
        (
            (51 49 53 55)
            (55 53 52 54)
            (54 52 48 50)
        );
    }
    side1
    {
        type cyclic;
        neighbourPatch side2;
        faces
        (
            (49 51 23 21)
            (21 23 3 1)
            (25 21 1 5)
            (27 25 5 7)
            (29 27 7 9)
            (9 7 41 43)
        );

        transform rotational;
        rotationAxis (0 0 1);
        rotationCentre (0 0 0);
        rotationAngle   #calc "$mrotAngle";

    }
    side2
    {
        type cyclic;
        neighbourPatch side1;
        faces
        (
            (48 20 22 50)
            (20 0 2 22)
            (24 4 0 20)
            (26 6 4 24)
            (28 8 6 26)
            (8 42 40 6)
        );
        transform rotational;
        rotationAxis (0 0 1);
        rotationCentre (0 0 0);
        rotationAngle   #calc "$rotAngle";

    }
);
mergePatchPairs
(
);
// ****************************************
```

## A.2. Pressure and Velocity

```
    object      p;
}
// * * * * * * * * * * * * * * * * * * *

dimensions      [0 2 -2 0 0 0 0];

internalField   uniform 0;

boundaryField
{
    wallStator
    {
        type            zeroGradient;
    }
    wallRotor
    {
        type            zeroGradient;
    }
    outlet
    {
        type            fixedValue;
        value           uniform 0;
    }
    inlet
    {
        type            zeroGradient;
    }
    side1
    {
        type            cyclic;
    }
    side2
    {
        type            cyclic;
    }
}
```

```
    object      U;
}
// * * * * * * * * * * * * * * * * * * * * * * *
dimensions      [0 1 -1 0 0 0 0];

internalField   uniform (0 0 0);

boundaryField
{
    wallStator
    {
        type            fixedValue;
        value           uniform (0 0 0);
    }
    wallRotor
    {
        type            rotatingWallVelocity;
        origin          (0 0 0);
        axis            (0 0 1);
        omega           constant 78.5;
        value           uniform (0 0 0);
    }
    outlet
    {
        type            inletOutlet;
        inletValue      uniform (0 0 0);
        value           uniform (0 0 0);
    }
    inlet
    {
        type            flowRateInletVelocity;
        volumetricFlowRate constant 0;
        extrapolateProfile 0;
        value           uniform (0 0 0);
    }
    side1
    {
        type            cyclic;
    }
    side2
    {
        type            cyclic;
    }
}
```

## A.3. *k*, *nut*, and *omega*

```
    object      k;
}
// * * * * * * * * * * * * * * * * * * * * * * * * * * * * * * * * * * * * * * *

dimensions      [0 2 -2 0 0 0 0];

internalField   uniform 0.147;

boundaryField
{
    wallStator
    {
        type            kqRWallFunction;
        value           uniform 0;
    }
    wallRotor
    {
        type            kqRWallFunction;
        value           uniform 0;
    }
    outlet
    {
        type            zeroGradient;
    }
    inlet
    {
        type            turbulentIntensityKineticEnergyInlet;
        intensity       0.0266;
        value           uniform 0.147;
    }
    side1
    {
        type            cyclic;
    }
    side2
    {
        type            cyclic;
    }
}
```

```
    object      omega;
}
// * * * * * * * * * * * * * * * * * * * * * * * * * * * * * * * * * * * * * * *

dimensions      [0 0 -1 0 0 0 0];

internalField   uniform 20000;

boundaryField
{
    wallStator
    {
        type            omegaWallFunction;
        value           uniform 20000;
    }
    wallRotor
    {
        type            omegaWallFunction;
        value           uniform 20000;
    }
    outlet
    {
        type            zeroGradient;
    }
    inlet
    {
        type            turbulentMixingLengthFrequencyInlet;
        mixingLength    3.5e-05;
        value           uniform 20000;
    }
    side1
    {
        type            cyclic;
    }
    side2
    {
        type            cyclic;
    }
}
```

```
    object      nut;
}
// * * * * * * * * * * * * * * * * * * * *

dimensions      [0 2 -1 0 0 0 0];

internalField   uniform 7.35e-06;

boundaryField
{
    wallStator
    {
        type            nutkWallFunction;
        value           uniform 0;
    }
    wallRotor
    {
        type            nutkWallFunction;
        value           uniform 0;
    }
    outlet
    {
        type            calculated;
        value           uniform 0;
    }
    inlet
    {
        type            calculated;
        value           uniform 7.35e-06;
    }
    side1
    {
        type            cyclic;
    }
    side2
    {
        type            cyclic;
    }
}
```

### A.4. RAS Properties and Turbulence Properties

```
    object      turbulenceProperties;
}
// * * * * * * * * * * * * * * * * * *

simulationType  RAS;

RAS
{
    RASModel         kOmegaSST;

    turbulence       on;

    printCoeffs      on;
}
```

```
    object      transportProperties;
}
// * * * * * * * * * * * * * * * * * * * * *

transportModel  Newtonian;

nu              [0 2 -1 0 0 0 0] 1.02e-06;
```

### A.5. ControlDict

```
    object      controlDict;
}
// * * * * * * * * * * * * * *

application     simpleFoam;

startFrom       startTime;

startTime       0;

stopAt          endTime;

endTime        2000;

deltaT          1;

writeControl    timeStep;

writeInterval   100;

purgeWrite      0;

writeFormat     ascii;

writePrecision  6;

writeCompression off;

timeFormat      general;

timePrecision   6;

runTimeModifiable true;
```

### A.6. fvSchemes

```
    object      fvSchemes;
}
// * * * * * * * * * * * * * * * * * * * * * * * * * * *

ddtSchemes
{
    default         steadyState;
}

gradSchemes
{
    default         cellLimited Gauss linear 1;

    limited         cellLimited Gauss linear 1;
    grad(U)         $limited;
    grad(k)         $limited;
    grad(omega)     $limited;
}
divSchemes
{
    default         none;

    div(phi,U)      bounded Gauss linearUpwindV grad(U);
    turbulence      bounded Gauss linearUpwind limited;
    div(phi,k)      $turbulence;
    div(phi,omega)  $turbulence;
    div((nuEff*dev2(T(grad(U))))) Gauss linear;
}
laplacianSchemes
{
    default         Gauss linear corrected;
}

interpolationSchemes
{
    default         linear;
}

snGradSchemes
{
    default         corrected;
}
wallDist
{
    method meshWave;
}
```

### A.7. fvSolution

```
    object      fvSolution;
}
// * * * * * * * * * * * * * * * * * * * *
solvers
{
    p
    {
        solver          GAMG;
        smoother        GaussSeidel;
        tolerance       1e-6;
        relTol          0.1;
    }

    "(U|k|omega)"
    {
        solver          smoothSolver;
        smoother        symGaussSeidel;
        tolerance       1e-6;
        relTol          0.1;
    }
}

SIMPLE
{
    nNonOrthogonalCorrectors 0;
    consistent      yes;


    residualControl
    {
        U                   1e-7;
        p                   1e-7;
        "(k|omega)"         1e-7;
    }
}
relaxationFactors
{
    equations
    {
        U                   0.95;
        "(k|omega)" 0.95;
    }
}
```

### A.8. decomposePar

```
    object      decomposeParDict;
}
// * * * * * * * * * * * * * * * *

numberOfSubdomains 6;

method          scotch;
```

```
    side1
    {
        type            cyclic;
        inGroups        List<word> 1(cyclic);
        nFaces          3336;
        startFace       1505376;
        matchTolerance  0.0001;
        neighbourPatch  side2;
        transformType   rotational;
        rotationAxis    (0 0 1);
        rotationCentre  (0 0 0);
        rotationAngle   -40;
    }
    side2
    {
        type            cyclic;
        inGroups        List<word> 1(cyclic);
        nFaces          3336;
        startFace       1508712;
        matchTolerance  0.0001;
        neighbourPatch  side1;
        transformType   rotational;
        rotationAxis    (0 0 1);
        rotationCentre  (0 0 0);
        rotationAngle   40;
    }
```

## B.1. The radial pressure distributions in three different gaps

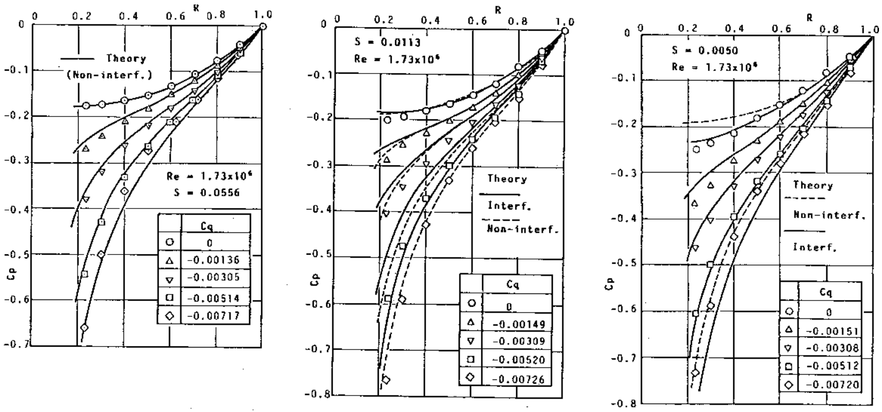


(a) $S$=0.0556. (b) $S$=0.0113 (c) $S$=0.0050

Fig. 6 Radial pressure distribution in the inward through-flow case

Radial pressure distribution for 3 different